



# 1 QBOi El Niño Southern Oscillation experiments: Assessing 2 relationships between ENSO, MJO, and QBO

3 Dillon Elsbury<sup>1,2</sup>, Federico Serva<sup>3</sup>, Julie M. Caron<sup>4</sup>, Seung-Yoon Back<sup>5</sup>, Clara Orbe<sup>6</sup>, Jadwiga H. Richter<sup>4</sup>  
4 James A. Anstey<sup>7</sup>, Neal Butchart<sup>8</sup>, Chih-Chieh Chen<sup>4</sup>, Javier García-Serrano<sup>9,10</sup>, Anne Glanville<sup>4</sup>, Yoshio  
5 Kawatani<sup>11,12</sup>, Tobias Kerzenmacher<sup>13</sup>, Francois Lott<sup>14</sup>, Hiroaki Naoe<sup>15</sup>, Scott Osprey<sup>16,17</sup>, Froila M.  
6 Palmeiro<sup>9,18</sup>, Seok-Woo Son<sup>5</sup>, Masakazu Taguchi<sup>19</sup>, Stefan Versick<sup>13</sup>, Shingo Watanabe<sup>20</sup>, Kohei  
7 Yoshida<sup>15</sup>

8  
9 <sup>1</sup> Cooperative Institute for Research in Environmental Sciences University of Colorado Boulder, Boulder, Colorado, USA

10  
11 <sup>2</sup> NOAA/Chemical Sciences Laboratory, Boulder, Colorado, USA

12  
13 <sup>3</sup> Institute of Marine Sciences, National Research Council (ISMAR-CNR), Rome, Italy

14  
15 <sup>4</sup> U. S. National Science Foundation National Center for Atmospheric Research (NSF NCAR), Boulder, CO, USA

16  
17 <sup>5</sup> School of Earth and Environmental Sciences, Seoul National University, Seoul, South Korea

18  
19 <sup>6</sup> NASA Goddard Institute for Space Studies (GISS), New York, New York, USA

20  
21 <sup>7</sup> Canadian Centre for Climate Modelling and Analysis (CCCma), Victoria, British Columbia, Canada

22  
23 <sup>8</sup> Met Office Hadley Centre, Exeter, United Kingdom

24  
25 <sup>9</sup> Group of Meteorology, Universitat de Barcelona, Barcelona, Spain

26  
27 <sup>10</sup> Barcelona Supercomputing Center (BSC), Barcelona, Spain

28  
29 <sup>11</sup> Faculty of Environmental Earth Science, Hokkaido University, Sapporo, Japan

30  
31 <sup>12</sup> Japan Agency for Marine-Earth Science and Technology, Yokohama, Japan

32  
33 <sup>13</sup> Institute of Meteorology and Climate Research-Atmospheric Trace Gases and Remote Sensing (IMK-ASF) Karlsruhe  
34 Institute of Technology (KIT), Karlsruhe, Germany

35  
36 <sup>14</sup> Laboratoire de Météorologie Dynamique (LMD), Paris, France

37  
38 <sup>15</sup> Meteorological Research Institute (MRI), Tsukuba, Japan

39  
40 <sup>16</sup> National Centre for Atmospheric Science (NCAS), United Kingdom

41  
42 <sup>17</sup> Department of Physics, University of Oxford, United Kingdom



43  
44 <sup>18</sup> CMCC Foundation - Euro-Mediterranean Center on Climate Change, Italy

45  
46 <sup>19</sup> Aichi University of Education, Kariya, Japan

47  
48 <sup>20</sup> Japan Agency for Marine-Earth Science and Technology (JAMSTEC), Yokohama, Japan

49  
50  
51 *Correspondence to:* Dillon Elsbury (dillon.elsbury@noaa.gov)

52 **Abstract.** This study uses an ensemble of climate model experiments coordinated by the Quasi-Biennial Oscillation initiative  
53 (QBOi) to analyze the Madden-Julian Oscillation (MJO) in the presence of either perpetual El Niño or La Niña sea surface  
54 temperatures during boreal winter. In addition to the prescribed El Niño Southern Oscillation (ENSO) conditions, the nine  
55 models internally generate QBOs, meaning each may influence the MJO. The diagnostics used include wavenumber-frequency  
56 spectra of tropical convective and dynamical fields, measures of MJO lifetime, an evaluation of MJO diversity and  
57 visualization of MJO vertical structure, as well as an assessment of QBO morphology and the QBO’s impact on tropical  
58 convection. Kelvin wave spectral power increases in the El Niño simulations whereas equatorial Rossby waves power is  
59 stronger in the La Niña simulations. Consistent with the reported relationship between these waves and the MJO, all models  
60 simulate faster MJO propagation under El Niño conditions. This change in speed is corroborated by the MJO diversity analysis,  
61 which reveals that models better reproduce the observed “fast propagating” and “standing” MJO archetypes given perpetual  
62 El Niño and La Niña, respectively. Regardless of ENSO, QBO descent into the lower stratosphere is underestimated and we  
63 detect little QBO influence on tropical tropopause stability and MJO activity. With little influence from the QBO on the MJO  
64 activity in these runs, we can be confident that the aforementioned changes in the MJO indeed arise from the different ENSO  
65 boundary conditions.

## 66 **1 Introduction**

67 The tropical circulation is influenced by various forms of internal variability, each operating at different timescales, yet still  
68 influencing each other. The Madden-Julian Oscillation (MJO) is dominant at intraseasonal timescales (Madden and Julian  
69 1994; Lin, 2022). It consists of large-scale eastward propagating fluctuations in tropical precipitation and circulation that  
70 traverse the Indian Ocean and Maritime Continent through to the Pacific over roughly 30 to 60 days (Hendon and Salby 1994).  
71 MJO variability fluctuates a lot year to year as does other variability in the climate system. At interannual timescales, the El  
72 Niño Southern Oscillation (ENSO; Philander, 1990) is one of the most important sources of tropical tropospheric variability.  
73 It is characterized by shifting patterns of sea surface temperatures (SSTs) and associated changes in ocean and atmospheric  
74 circulations in the tropical Pacific. ENSO varies on timescales between two to seven years, and consists of three phases, the  
75 warm El Niño, the cold La Niña and a “neutral” phase where neither polarity dominates. Also operating at interannual  
76 timescales is the Quasi Biennial Oscillation (QBO), which is the dominant mode of variability in the lower tropical



77 stratosphere, defined by alternating easterly and westerly shear zones descending from 5 to 100 hPa with an average periodicity  
78 of 28 months (Baldwin et al. 2001).

79  
80 The three described oscillations, ENSO, QBO, and MJO, have been shown to influence each other in multiple ways. ENSO's  
81 La Niña and El Niño phases are associated with shifts of intraseasonal tropical atmospheric variability like the MJO towards  
82 the Indo-Pacific Warm Pool and Date Line, respectively (Kessler 2001; Tam and Lau 2005). In addition, ENSO can influence  
83 the amount of time the MJO spends in particular Wheeler and Hendon (2004) MJO phases and the duration of MJO events  
84 overall, which are shorter during El Niño and longer during La Niña (Pohl and Matthews 2007; Pang et al. 2016; Wei and Ren  
85 2019; Wang et al. 2019; Dasgupta et al. 2021; Fernandes and Grimm 2023).

86  
87 Despite these apparent sensitivities of the MJO to ENSO, there is also convincing evidence that the relationship between  
88 seasonal mean MJO activity and ENSO is weak (Lin 2022). Slingo et al. (1999) found that the observed intraseasonally filtered  
89 zonal mean 200 hPa zonal wind (their metric of "MJO activity") is weakly dependent on ENSO phase. They affirmed this  
90 further by using an ensemble of AMIP simulations. Hendon et al. (1999) validated and refined their definition of MJO activity,  
91 finding it to capture the salient features of the MJO and again that its variability is mostly independent of ENSO. These results  
92 also align with those of Newman et al. (2009) who showed that air-sea coupling has a small effect on intraseasonal atmospheric  
93 variability in empirical models that run with and without atmosphere-ocean interaction. With these results in mind, it is less  
94 clear how the MJO should respond to the ENSO conditions prescribed in our simulations. In fact, a common idea amongst the  
95 studies just mentioned is that the MJO's interannual variability originates predominantly from internal atmospheric processes  
96 other than those associated with ENSO.

97  
98 It is increasingly recognized that the easterly and westerly phases of the QBO exert an influence on the MJO (Yoo and Son,  
99 2016; Son et al. 2017; Sakaeda et al. 2020; Martin et al. 2021; Jin et al. 2023; Huang et al. 2023). The MJO's amplitude is  
100 stronger during easterly QBO boreal winters compared to westerly QBO winters over the observed record since 1979 (Yoo  
101 and Son 2016; Densmore et al. 2019). However, despite improvement in the representation of simulated QBOs (Richter et al.  
102 2020) and MJOs (Ahn et al. 2020) across model generations, current Earth system models generally do not simulate the QBO-  
103 MJO relationship (Kim et al. 2020; Lim and Son 2020; Martin et al. 2023), nor do they simulate a sufficiently strong tropical  
104 tropopause response to the QBO (Serva et al. 2022). Attempts to understand this deficiency are further complicated by a  
105 curious tendency for easterly QBO boreal winters to overlap with La Niña winters during the short observational record  
106 (Randall et al. 2023). For this reason, more process level understanding of how the ENSO and the QBO influence the MJO is  
107 needed, which we pursue here using unique coordinated model experiments.

108  
109 We examine the influence of ENSO and the QBO on the MJO using a multi-model ensemble of experiments with perpetual  
110 El Niño and La Niña conditions in nine global models that internally generate QBOs. These simulations were coordinated by



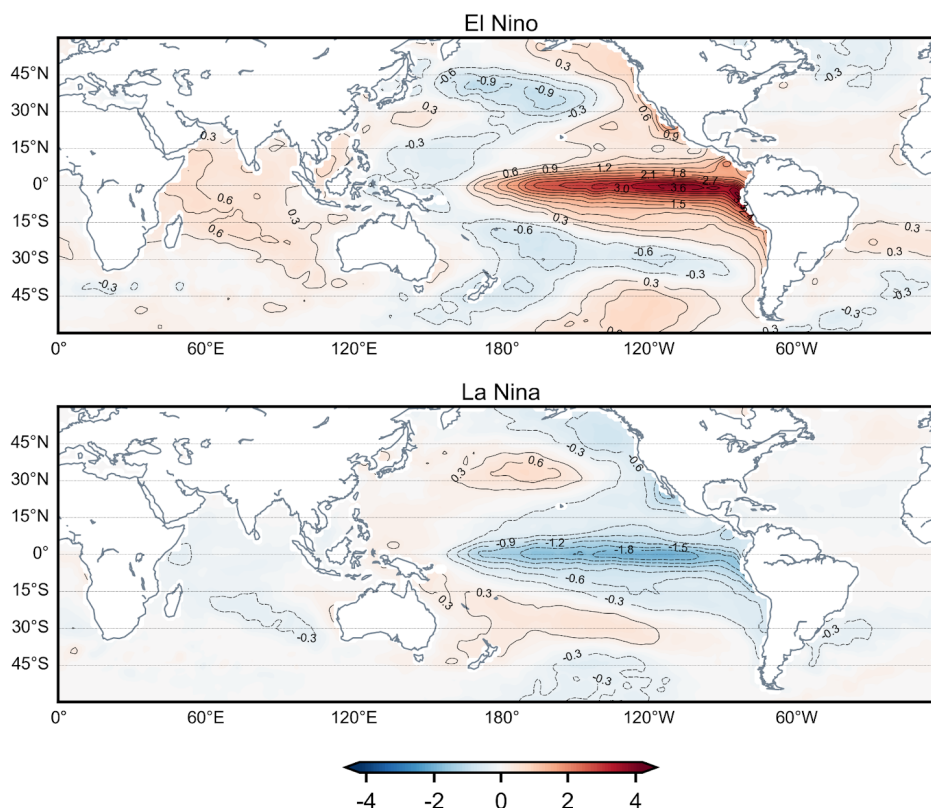
111 the Atmospheric Processes And their Role in Climate (APARC, previously “SPARC”) Quasi-Biennial Oscillation initiative  
112 (QBOi), which seeks to improve the fidelity of tropical stratospheric variability in general circulation and Earth system models  
113 through coordinated multi-institutional climate model experiments (Butchart et al. 2018). The perpetual-ENSO experiments  
114 used here are a continuation of the QBOi Phase 1 experiments and have companion studies that examine ENSO’s effect on the  
115 QBO (Kawatani et al., in preparation) and the combined influence of ENSO and the QBO on global teleconnections (Naoe et  
116 al., in preparation).

## 117 **2 Methods**

### 118 **2.1 Experimental setup**

119 Butchart et al. (2018) established a set of simplified modeling experiments for Phase 1 of the QBOi. Their Experiment 2, the  
120 “present-day time slice” simulation, forms the basis for these perpetual ENSO simulations. It was designed to allow for an  
121 evaluation of the accuracy of modeled QBOs under present-day conditions, that is, how the model QBOs operate in a climate  
122 forced with fixed repeating annual cycles of global sea surface temperature (SSTs), sea ice concentration (SIC), and external  
123 forcings representative of the time averaged 1988-2007 state.

124  
125 The perpetual ENSO runs analyzed here are equivalent to Experiment 2, but with global El Niño or La Niña SST anomalies  
126 superimposed on top of the climatological SST forcing. An assessment of the MJO is not conducted for Experiment 2 because  
127 essential variables such as daily horizontal winds, outgoing longwave radiation (OLR), and precipitation, were not archived.  
128 In creating the composite El Niño or La Niña forcings, the characterization of ENSO follows the Japan Meteorological Agency  
129 (JMA) convention, where ENSO is defined by the spatially averaged NINO.3 (5°S-5°N,150°W-90°W) monthly SST anomalies  
130 from 1950-2016. Anomalies are defined as deviations from the climatological seasonal cycle and computed relative to the  
131 most recent sliding 30-year period of JMA COBE-SST version 1 data (JMA, 2006). The anomalies are smoothed using a five-  
132 month running mean and the periods during which the anomalies exceed 0.5°C (-0.5°C) for at least six consecutive months  
133 are labeled as El Niño (La Niña) periods. However, after averaging the SST anomalies for all El Niño Januarys, Februarys,  
134 etc., and doing the same for La Niña, the composite average annual cycles of El Niño and La Niña SSTs show only modest  
135 amplitudes (e.g., 1.92 °C for El Niño Januarys). To amplify the atmospheric response to ENSO in the simulations, the annual  
136 cycles are multiplied by 1.8 and 1.4, respectively, making their amplitudes comparable to the strongest observed ENSO events.  
137 A similar scaling is applied to the corresponding global signatures in NINO.3 SST anomalies (Fig. 1), which are superimposed  
138 on 1988–2007 climatological SSTs and prescribed in the models. Note that this procedure does not completely capture the  
139 development, mature phase, and decay of all observed El Niño events, due to diversity in the evolutions of events.



140

141 **Figure 1: November-April composites of the El Niño and La Niña JMA COBE SST anomalies that are prescribed in the perpetual**  
 142 **ENSO simulations.**

143 In addition to the prominent El Niño and La Niña signals, the November-April (NDJFMA) SSTs shown in Figure 1 include  
 144 the signatures of the basin-scale Interdecadal Pacific Oscillation (IPO) (Henley et al. 2015) and Indian Ocean SSTs that are in  
 145 phase with ENSO. In some regions like the tropical Pacific and Indian Oceans, the amplitude of the global SSTs associated  
 146 with the El Niño (Fig. 1b) are roughly double that of La Niña (Fig. 1a).

147

148 **2.2 Models**

149

150 *Table 1: The models used in this study, the number of years per simulation, and some relevant literature. Only one realization is used from*  
 151 *each model.*

Model	Number of years	Convective parameterizations
EC-EARTH3.3	101	Bechtold (2014)



ECHAM5sh	40	Tiedkte (1989), Nordeng (1994)
EMAC	106	Tiedkte (1989)
LMDz6	80	Emanuel (1991), Hourdin et al. (2013)
GISS-E2-2-G	30	Rind et al. (2020); Kelley et al. (2020)
MIROC-AGCM-LL	100	Pan and Randall (1998); Emori et al. (2001)
MIROC-ESM	100	Pan and Randall (1998); Emori et al. (2001)
MRI-ESM2.0	50	Yukimoto et al. (2019)
CESM1(WACCM5-110L)	101	Zhang and McFarlane (1995)

152

153 The models considered in this work are listed in Table 1 along with the number of years analyzed for each model and references  
 154 on each model’s convective parameterization. These parameterizations impact the representation of tropical phenomena (Holt  
 155 et al. 2020; Kawatani et al., in preparation), including the simulation of intraseasonal oscillations (Ham and Hong, 2013). For  
 156 example, past sensitivity tests with the version of MIROC-ESM that we use here have shown that its cumulus parameterization  
 157 struggles to simulate an MJO of realistic amplitude with capability to propagate over the Maritime Continent (Miura et al.  
 158 2012). The updated scheme (Chikira and Sugiyama 2010) in use in newer versions of the model, MIROC6, has helped  
 159 ameliorate these issues (Ahn et al. 2017; 2020). The importance of simulated convection-circulation coupling has been  
 160 identified for other models (Kim et al. 2014; Zhu et al. 2020; Wang et al. 2022).

161 **2.3 Observation-based reference data**

162 To be consistent with previous studies (Wei and Ren 2019), the ENSO-MJO relationship is considered during November to  
 163 April. The six observed La Niña years, where the year is associated with November, are 1970, 1984, 1988, 2017, 2020, and  
 164 2021 and the eight El Niño years are 1968, 1982, 1986, 1991, 1997, 2009, 2015, 2018. Each corresponds to an instance when  
 165 the smoothed NINO.3 anomalies exceed +/- 0.5C for at least six consecutive months. For comparison with the models, the  
 166 subsequent analyses include “observed” El Niño and La Niña composites, formed by averaging deseasonalized 1959-2022  
 167 ERA5 reanalysis (Hersbach et al. 2020) over the aforementioned years. These El Niño and La Niña composites are not scaled  
 168 by factors of 1.8 and 1.4, respectively, in contrast to the ENSO SSTs prescribed in the simulations. Hence the ERA5 responses  
 169 are expected to be more modest in amplitude compared with responses from the models. However, the difficulties that the  
 170 models have simulating the MJO in some respects can render this untrue in practice.





171

172 Building on the analysis of the ENSO-MJO relationship, it is also important to consider other atmospheric phenomena such as  
173 the QBO. The QBO-MJO relationship in the models is analyzed during December through February for consistency with  
174 previous studies (e.g., Son et al. 2017).

## 175 2.4 MJO analyses

176 We implement a number of widely-used methods to evaluate the MJO in the perpetual ENSO simulations. In the interest of  
177 exploring changes to MJO lifetime by ENSO phase as well as visualizing the MJO's vertical structure, we compute Real-time  
178 Multivariate MJO indices (RMMs) for each perpetual ENSO simulation using the same methodology as Wheeler and Hendon  
179 (2004, WH04). The RMMs are derived from a combined empirical orthogonal function (EOF) analysis of tropically averaged  
180 ( $15^{\circ}\text{S}$ - $15^{\circ}\text{N}$ ) anomalous daily outgoing longwave radiation (OLR), 200-hPa zonal wind (U200), and 850-hPa zonal wind  
181 (U850). As in WH04, we deseasonalize, remove interannual variability, and normalize the anomalies by their global variance.  
182 To enable a fairer comparison between the models and reanalysis, we project the anomalous model fields onto the 1959-2022  
183 ERA5 WH04 EOFs; projecting onto each model's respective ENSO simulation instead does not change the conclusions. Daily  
184 OLR and U200 were not available for two models (GISS-E2-2-G and LMDz6) so their RMMs are computed using U250 and  
185 U850. The number of MJO events within a given data set is tallied like in Pohl and Matthews (2007) by counting the number  
186 of times the MJO makes a complete rotation through its RMM1 and RMM2 phase space. Average lifetime and MJO amplitudes  
187 ( $\sqrt{RMM1^2 + RMM2^2}$ ) are computed across events. To visualize the MJO's vertical structure, latitudinally averaged  $10^{\circ}\text{S}$ -  
188  $10^{\circ}\text{N}$  longitude-pressure cross-section of zonal wind and temperature are projected onto the RMMs using the same steps as  
189 Hendon and Abhik (2018), but applied across ENSO years in the present study rather than QBO years.

190

191 The MJO is also visualized using two slightly different wavenumber-frequency filtering analyses. The first, available via the  
192 MJO US Climate Variability and Predictability (CLIVAR) metrics package (Waliser et al. 2009), is computed by Fourier  
193 transforming in time and longitude deseasonalized, tapered, and centered November-April segments of tropical OLR and  
194 U850, reorganizing the Fourier coefficients for eastward and westward disturbances (Hayashi 1982) and computing power,  
195 Figures 3 and 4 respectively. The second filtering technique is broadly similar, but specializes in resolving convectively  
196 coupled waves in addition to the MJO (Wheeler and Kiladis 1999). Prior to this analysis, the multi-year daily-mean fields from  
197 ERA5 and each model are linearly detrended, high pass filtered for intraseasonal variability using a 96-day cutoff, grouped  
198 into 96-day segments that share 65 days of overlap with neighboring segments, and each segment is linearly detrended and  
199 tapered. Successive discrete Fourier transforms are applied in longitude and time, the coefficients are reordered (Hayashi  
200 1982), we retrieve the symmetric and antisymmetric components of a given field's spectra with respect to the equator and then  
201 divide each component by a smoothed background spectrum. The resulting power spectrum, shown as the ratio between raw  
202 symmetric daily-mean precipitation power and the background spectrum in Figure 2, reveals the modes of organized



203 convection with the most power. Model spectra are divided by their respective perpetual ENSO backgrounds, whereas ERA5  
204 El Niño and La Niña spectra are both compared to the 1959-2022 background; conclusions from ERA5 results are not sensitive  
205 to using respective El Niño or La Niña backgrounds.

206  
207 We also implement an MJO diversity analysis in which MJO events are classified into distinct types based on their propagation  
208 characteristics using k-means clustering (Wang et al. 2019). Each MJO event is binned as one of four archetypes, “standing”  
209 or “jumping” MJOs, which propagate across the Indian Ocean, but are distinguished by reemergence of the MJO over the  
210 western Pacific during jumping events, and “slow” or “fast” MJOs, which both continuously propagate across the Maritime  
211 Continent, but at different speeds. An MJO event occurs when the 20-70 day bandpass-filtered OLR anomalies (from seasonal  
212 cycle) averaged over the equatorial Indian Ocean (10°S-10°N, 75°E-95°E) are smaller than negative one standard deviation  
213 for five successive days; the reference day (day 0) is the day of minimum OLR. The MJO events are categorized by a k-means  
214 clustering of the enhanced convective signal (OLR anomalies under  $-5 \text{ Wm}^{-2}$ ) of the latitudinally averaged 10°S to 10°N time-  
215 longitude OLR anomalies taken over 60°E to 180°E and over a 31-day period from day -10 to day 20. For brevity, we omit  
216 further diversity analysis methodological details, for which we refer the reader to Back et al. (2024) for all steps. However, it  
217 is important to note that unlike Wang et al. (2019), in which initial centroids for clustering are randomly chosen, initial  
218 centroids for model MJO events are set to those of the four observation-based clusters to minimize subjective decisions.  
219 Because of this step, herein the present study evaluates how well the climate models can reproduce the observed MJO diversity  
220 archetypes.

## 221 **2.5 QBO and analyses**

222 The space-time form of the QBOs varies from model to model as each is generated with different amounts of forcing from  
223 resolved waves and parameterized non-orographic gravity wave drag. Properties of these models that are particularly relevant  
224 for simulating the QBOs are listed in Butchart et al. (2018), details on QBO morphology (e.g., its amplitude, latitudinal width)  
225 given the observed SST record are presented in Bushell et al. (2022), and the relative contribution of resolved and  
226 parameterized tropical waves to forcing the QBO is analyzed in detail in Holt et al. (2020). Of note, MIROC-AGCM-LL’s  
227 QBO is forced solely by resolved waves. As EC-EARTH and GISS-E2-EG did not contribute to some of the earliest QBO  
228 analyses, relevant details on their internal QBOs can be found in Serva et al. (2024) and Rind et al. (2014, 2020), respectively.  
229 For a thorough analysis of how the QBO responds to the perpetual ENSO simulations, we refer the reader to Kawatani et al.  
230 (in preparation).

231  
232 To help clarify the ability of the QBOs to interact with the MJOs, we use established metrics to characterize the morphology  
233 of the ERA5 and model QBOs. The main field used to document QBO morphology is the monthly zonal-mean zonal wind.  
234 “QBO cycles” (consecutive easterly/westerly phases) are identified by marking the first month when the deseasonalized and





235 smoothed (5-month running mean) 20 hPa 5°S-5°N wind changes from westerly to easterly, ending one month before the next  
236 transition at 20 hPa (Kawatani et al. 2019). From these cycles, we calculate average QBO easterly, westerly, and total  
237 amplitudes using the QBO “transition time” methodology of Richter et al. (2020). The easterly (westerly) amplitude is equal  
238 to the average of the minimum (maximum) monthly QBO winds from each QBO cycle. The QBO cycles are used further to  
239 calculate minimum, mean, and maximum QBO periodicity statistics. These statistics are a key result of Kawatani et al. (in  
240 preparation) and are discussed thoroughly there. In short, the periodicity of the QBO decreases in all El Niño simulations and  
241 increases in all La Niña simulations. For the purposes of the present study, the minimum and maximum periodicities are  
242 required to evaluate the QBO’s spatial structure, defined as the latitude-pressure cross sections of each data set’s QBO Fourier  
243 amplitude. These are made by applying a discrete Fourier transform in time to the multi-year monthly zonal-mean zonal wind  
244 at each pressure-latitude grid point and dividing the sum of squares of the amplitudes of the harmonics corresponding to periods  
245 between the minimum and maximum QBO periods by the sum of squares of the amplitudes of all harmonics. This ratio is  
246 subsequently multiplied by the standard deviation of the zonal-mean zonal wind (Pascoe et al. 2005). Using this QBO Fourier  
247 amplitude, the lowest altitude the QBO reaches, its vertical extent (i.e., how tall it is), and its latitudinal extent are defined as  
248 in Schenzinger et al. (2017), except that here the QBO’s maximum amplitude is assumed to be at 20 hPa for all models and  
249 ERA5.

250

251 The QBO’s capability to impact the tropical tropopause and the MJO is further assessed using the techniques of Klotzbach et  
252 al. (2019) and Kim et al. (2020). Following the prior, we make scatterplots of December-February warm-pool (10°S-10°N,  
253 45°E-180°E) averaged tropopause stability (100 hPa minus 200 hPa temperature) versus December-February MJO amplitude  
254 as a function of QBO phase (sign of DJF averaged 5°S-5°N 50 hPa zonal mean zonal-wind) for each of the simulations. MJO  
255 amplitude is expected to increase as tropopause stability decreases, which happens during the easterly QBO phase. As in Kim  
256 et al. (2020), MJO activity is also computed as a function of QBO phase. Specifically, MJO-filtered OLR is calculated  
257 following Wheeler and Kiladis (1999) with one exception, the full time series is detrended rather than using 96-day overlapping  
258 segments. To minimize spectral leakage, 5% of the data are tapered to zero at the ends of the timeseries. After tapering, a  
259 complex Fourier Transform is performed, and the spectral wavenumber-frequency data are filtered to retain only the eastward  
260 propagating coefficients for 20-100 day periods and wavenumbers 1-5. MJO activity is then defined as the standard deviation  
261 of the MJO-filtered OLR across all December-February days that fall into a particular category, for instance all years, easterly  
262 QBO years or westerly QBO years. For this analysis, easterly and westerly QBO years are defined as those which exceed +/-  
263 0.5 standard deviation of the 50 hPa monthly zonal wind anomalies, seasonally smoothed and averaged over 10°S to 10°N.  
264 One may notice that the QBO is defined differently between the Klotzbach and Kim et al. analyses. Herein, we have prioritized  
265 using the aforementioned metrics in their original form rather than using customized metrics so as to have one uniform  
266 definition of, for instance, QBO phase.



## 267 **3 Results**

### 268 **3.1 ENSO-MJO coupling**

269 Before examining the influence of ENSO on MJO, we evaluate some of the other large-scale tropical phenomena that the  
270 models simulate. Convectively coupled waves are relevant because they comprise the space-time structure of the MJO and can  
271 influence its propagation by modulating the tropical circulation and the distribution of moisture that the MJO encounters  
272 (Kiladis et al. 2009; Wang et al. 2019; Wei and Ren 2019; Berrington et al. 2022; Wang and Li 2022). Aspects of the waves,  
273 such as their phase speed, vary depending on the low frequency circulation (Roundy 2012). Hence, the amplification of the  
274 Walker Circulation by La Niña and the weakening of it by El Niño (Fig. S1) provide a pathway for the perpetual ENSO  
275 forcings to modulate the waves and perhaps the MJO. Applying similar methods to Wheeler and Kiladis (1999), we visualize  
276 the waves by computing the spectral power of ERA5 and model daily-averaged precipitation as a function of wavenumber and  
277 frequency. Figure 2 shows the precipitation spectra for phenomena symmetric about the equator, taken over November-April  
278 and 15°S-15°N. Three dispersion curves, as in Matsuno (1966), corresponding to equivalent depths of 10, 25, and 50 meters  
279 are also superimposed; these curves are derived using the dispersion relations for equatorially trapped waves and they are co-  
280 located with modes of organized convection, with larger equivalent depths corresponding to faster phase speeds.

281  
282 Only six La Niña and eight El Niño events are used to make the ERA5 equivalent figures that are shown in row one, which  
283 coincides with these signals being noisy compared to the multi-decade averages from the models. Spectral signals associated  
284 with the eastward propagating Kelvin wave move up and to the right on each panel, spanning sub-planetary low frequency (~  
285  $k = 3, 25$  days) scales to synoptic ( $k = 4+$ ) sub-weekly scales. Relative to ERA5, the models underestimate the strength of the  
286 Kelvin wave and this happens irrespective of the type of ENSO forcing. Power associated with the westward propagating  
287 equatorial Rossby wave is evident on the left side of each panel between wavenumbers 1-10 and timescales of 10 days to five  
288 weeks. Overall, the models do a reasonable job of simulating the spectral amplitude of equatorial Rossby waves, although it is  
289 too strong for some models (EMAC, MIROC-ESM), especially in their La Niña simulations.

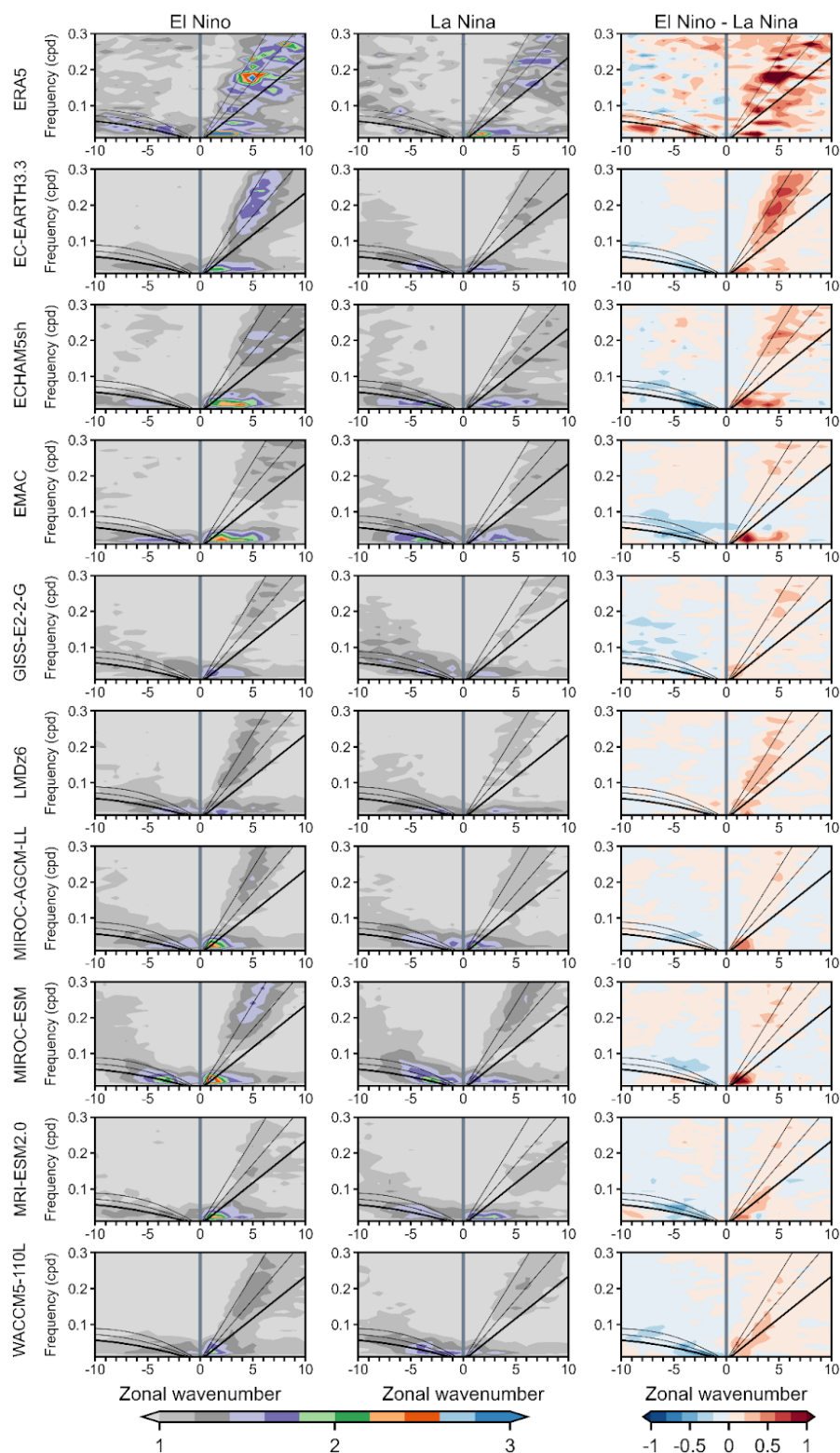
290



291

292 **Figure 2: Wavenumber-frequency power spectrum of the symmetric component of 15°S-15°N**  
 293 **November-April precipitation plotted as the ratio between raw symmetric precipitation power and a**  
 294 **smoothed red noise background spectrum. The eastward (right) side of the spectrum includes three**  
 295 **Kelvin wave dispersion curves in black, of which the thickest curve corresponds to the equivalent**  
 296 **depth of 12 meters, and the other two correspond to 25 and 50 meters, respectively. Similar**  
 297 **dispersion curve plotting conventions are used on the westward (left) side of the spectrum where the**  
 298 **curves overlay the equatorial Rossby wave power. Column one corresponds to El Niño, column two to**  
 299 **La Niña, and column three to their difference, which is computed as (El Niño symmetric minus El**  
 300 **Niño background) minus (La Niña symmetric minus La Niña background). Computing the third**  
 301 **column as (El Niño symmetric) minus (La Niña symmetric) yields similar conclusions (not shown).**  
 302  
 303  
 304  
 305  
 306  
 307  
 308  
 309  
 310  
 311  
 312

313 The effect of ENSO phase on each wave is  
 314 revealed by the rightmost column of Figure 2,  
 315 which shows El Niño (column one) minus La  
 316 Niña (column two) differences, where red means  
 317 stronger power during El Niño and blue means  
 318 larger power during La Niña. All models  
 319 simulate stronger Kelvin waves in their El Niño  
 320 simulation, particularly along the deeper  
 321 equivalent depth ( $n = 25, 50$  meters) dispersion  
 322 curves. This implies faster Kelvin wave phase  
 323 speeds during El Niño. Examining the El Niño  
 324 column, the alignment of the Kelvin wave power  
 325 along these particular curves is demonstrated by  
 326 EC-EARTH3.3, GISS-E2-E-G, LMDz6,  
 327 MIROC-AGCM-LL, MIROC-ESM, MRI-  
 328 ESM2.0 and (CESM1) WACCM5-110L,  
 329 hereafter just “WACCM5-110L.” The remaining  
 330 models, ECHAM5sh and EMAC (both ECHAM-  
 331 based models), differ in that their El Niño Kelvin  
 332 wave power is weighted towards higher zonal





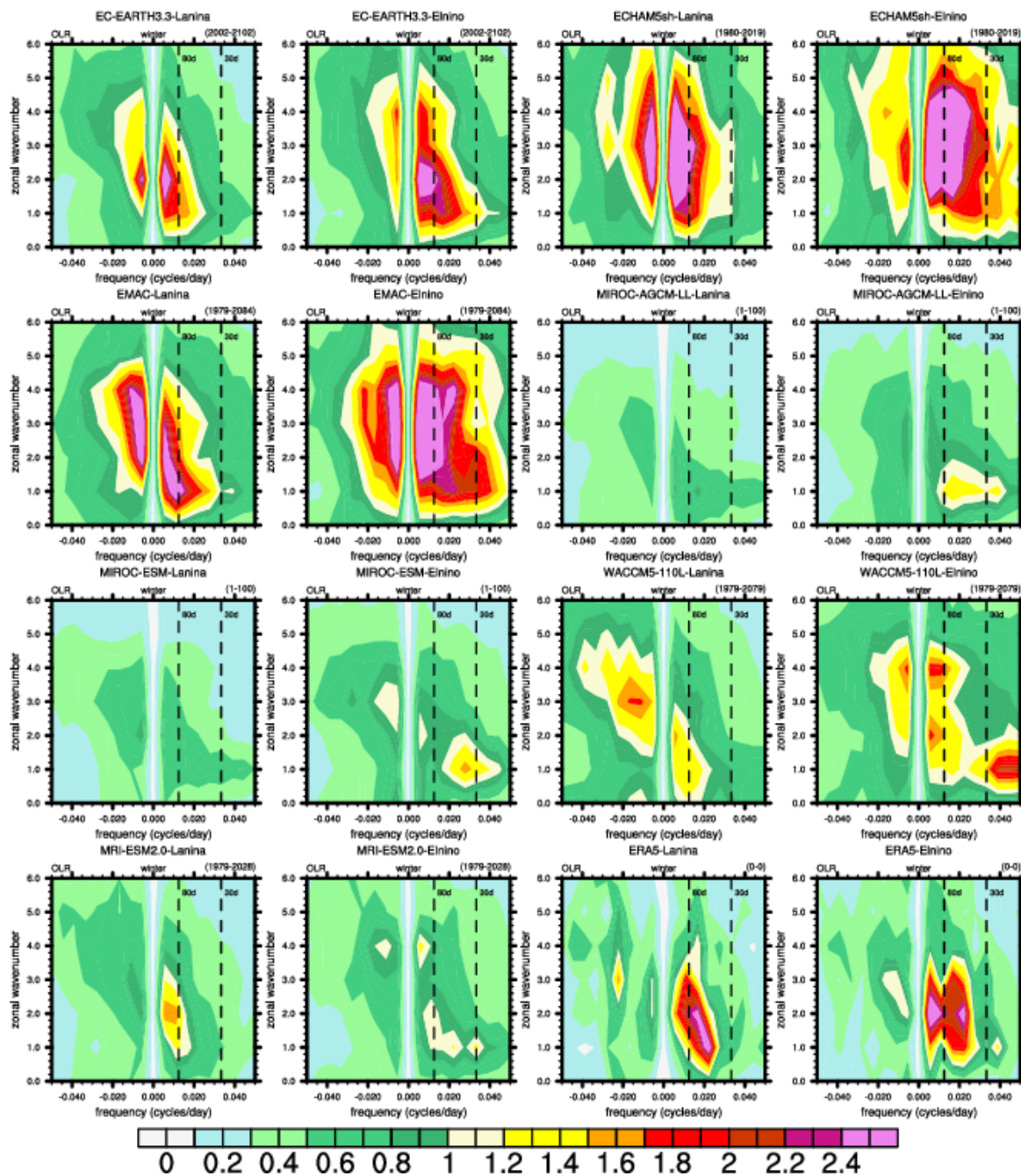
333 wavenumbers for frequencies below 0.2 cpd. Similar to the models, ERA5 shows large sporadic increases in Kelvin wave  
334 power along deeper equivalent depth dispersion curves during El Niño compared to La Niña. Agreement between ERA5 and  
335 the models is less clear when instead considering the westward propagating equatorial Rossby wave. All models simulate  
336 stronger equatorial Rossby wave power during La Niña. There is a tendency in some models for this to happen along the deeper  
337 equivalent depth dispersion curves (e.g., MIROC-AGCM-LL, MIROC-ESM).

338  
339 Having found changes in the convectively coupled waves due to ENSO, perhaps the model MJOs are also modulated by ENSO.  
340 Broadly speaking, Figure 2 shows that the models do in fact include MJOs as indicated by the maxima in spectral power at  
341 intraseasonal timescales ( $\ll 0.1$  cpd) between eastward propagating wavenumbers 1-5. Holt et al. (2020) also found MJOs to  
342 be simulated by these models. The highest MJO power in ERA5 is concentrated between wavenumbers 1 and 3 irrespective  
343 of ENSO phase. EC-EARTH3.3, MIROC-AGCM-LL, MIROC-ESM, MRI-ESM2.0 are closest to reproducing this whereas  
344 ECHAM5sh, EMAC, and LMDz6 exhibit spectral power that is incorrectly shifted towards higher wavenumbers. The El Niño  
345 minus La Niña differences shown in the rightmost column of Figure 2 highlight that MJO spectral power is stronger in the  
346 presence of the El Niño basic state, predominantly between wavenumbers 2 and 3 in ERA5 and wavenumbers 1 and 2 across  
347 the majority of the models. Differing from the other models, EC-EARTH3.3, ECHAM5sh, and EMAC have fairly large El  
348 Niño minus La Niña MJO power differences at wavenumber 4 and 5.

349  
350 Irrespective of ENSO phase, the amplitude of the model MJOs as shown in Fig. 2 is systematically weaker than in ERA5. This  
351 may have something to do with dividing each simulation's symmetric power by its respective background power, the latter of  
352 which is contaminated, in a sense, by the perpetual ENSO conditions. Note that recomputing the third column of Fig. 2 without  
353 dividing each El Niño and La Niña composite by their respective background does not change our conclusions (not shown).  
354 To get around this potential issue with the background power and further inspect the model MJOs as opposed to the  
355 convectively coupled waves, in Figures 3 and 4 we consider the westward and eastward wavenumber-frequency spectra of  
356 OLR and U850, respectively, taken over the intraseasonal timescale and over MJO-like zonal wavenumber scales. These  
357 analyses yield more holistic views of the MJO than in Fig. 2 because they incorporate the MJO's signals in these fields that  
358 are both symmetric and antisymmetric about the equator.

359





360

361

362

363

364

365

366

**Figure 3:** November-April wavenumber-frequency power spectra of 10°S-10°N averaged OLR. Units of the OLR spectrum are  $W^2/m^4$  per frequency interval per wavenumber interval.

Observed variance associated with convective fields like OLR predominantly spans zonal wavenumber 1-3 and frequencies corresponding to periodicities of 1-3 months (Hendon and Salby 1994). Independent of the ENSO phase, ERA5's wavenumber-frequency shows the highest power between wavenumbers 1-3 and frequencies of 30-80 days (vertical dashes),



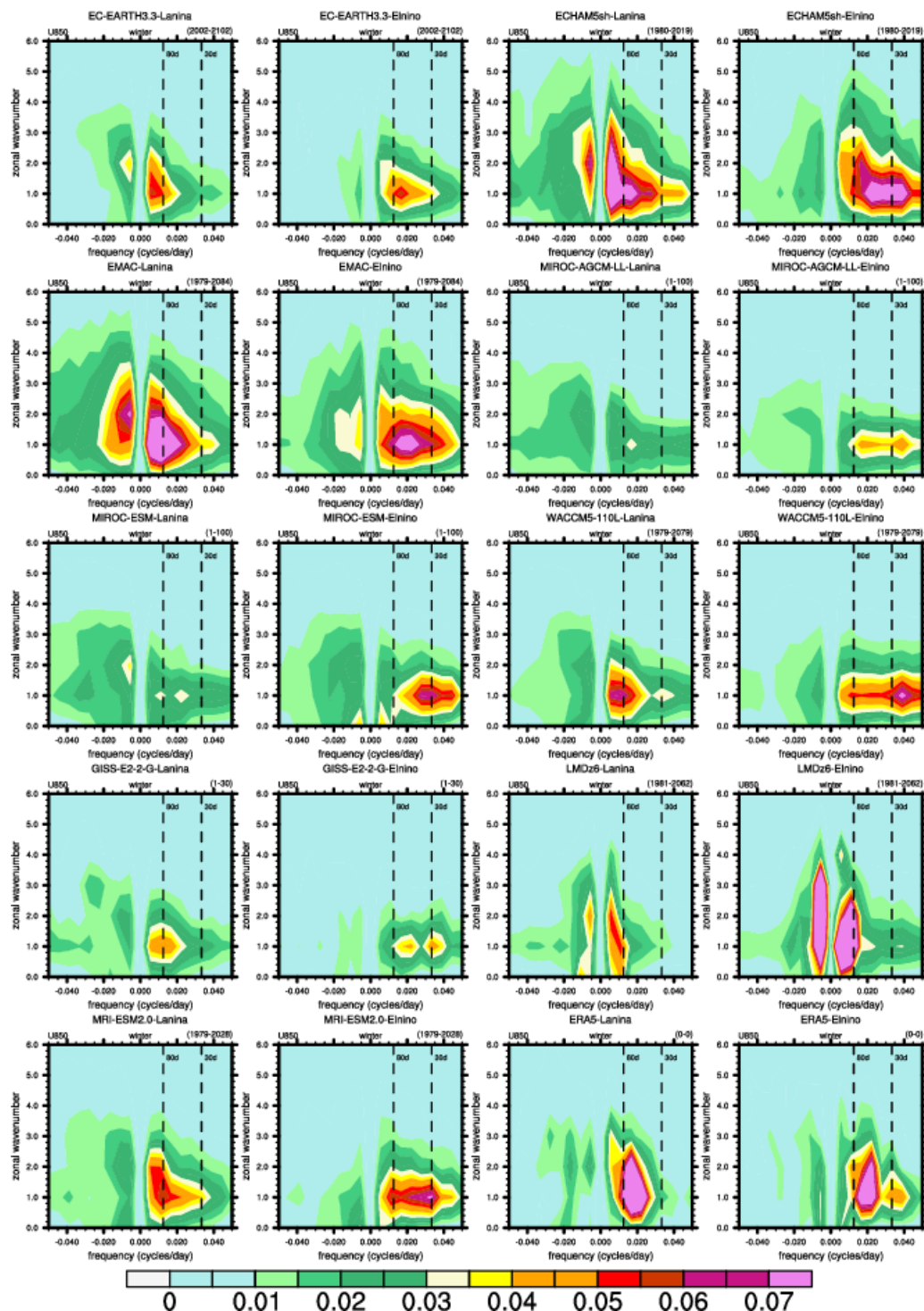
367 a so-called “MJO band” (Ahn et al. 2017). Considering only the MJO band, the MJO is stronger given lower zonal  
368 wavenumbers and longer periodicities during La Niña compared to El Niño. Despite La Niña having higher power at lower  
369 frequencies within the MJO band, it is actually El Niño that has larger spectral power beyond 80 days, which we conjecture  
370 reflects the diversity of El Niño’s influence on the MJO (Wei and Ren 2019). There is also strong power at frequencies  
371 corresponding to periods of 181 days, especially in the ERA5 El Niño composite, which is likely an artifact of using 181-day  
372 NDJFMA segments for this analysis.

373

374 There are notable differences in the amplitude of the spectral power between each model and ERA5 for both El Niño and La  
375 Niña. Of the models, EC-EARTH3.3’s MJO band amplitude is most similar to ERA5. MIROC-AGCM-LL, MIROC-ESM,  
376 and WACCM5-110L significantly underestimate the strength of the MJO in this metric whereas ECHAM5sh and EMAC both  
377 overestimate it. Another issue is that the models consistently exhibit too large of an MJO signal for zonal wavenumbers three  
378 and up, which is unrealistic and common amongst GCMs (Ahn et al. 2017). When MJO power is considered as a function of  
379 ENSO phase, all models show that the MJO is stronger during El Niño, especially near the high frequency portion of the MJO  
380 band.

381





382

383

Figure 4: Same as Figure 3, but for U850 across all nine models and ERA5.



384 As shown by ERA5, the MJO timescale variance of dynamical fields such as U850 is known to have a much narrower spectral  
 385 peak around zonal wavenumber-1 (Fig. 4). The models are fairly good at reproducing this. Using U850 allows us to incorporate  
 386 output from GISS-E2-2-G and LMDz6 for which OLR data is not available. Notwithstanding some of the typical model issues  
 387 (e.g., amplitude differences compared to observations, and overly large power at high wavenumbers especially in ECHAM5sh,  
 388 EMAC, and LMDz6), Figure 4 like Figure 3 indicates that the periodicity of the MJO decreases during El Niño and increases  
 389 during La Niña. The robustness of these results is considered further by using the PM07 MJO statistics including MJO lifetime,  
 390 which are tabulated in Table 2.

391  
 392 *Table 2: The number of MJO events, their mean lifetimes and standard errors (reported in parentheses), and their mean amplitudes given*  
 393 *either perpetual El Niño or La Niña conditions in a model. An asterisk (\*) next to a model name indicates that the RMMs were retrieved*  
 394 *using only 250 and 850 hPa zonal wind. Different from the models, for ERA5, MJO event statistics are calculated using 8 El Niño and 6 La*  
 395 *Niña winters subsampled from the entire 1959-2022 RMM record.*

396

	EN events (#/dec)	LN events (#/dec)	EN lifetime (days)	LN lifetime (days)	EN amplitude	LN amplitude
ERA5	25	22	38.25 (2.27)	47.07 (3.97)	1.36	1.41
EC-EARTH3.3	18.07	13.80	37.96 (1.25)	46.73 (2.01)	1.47	1.40
ECHAM5sh	26.20	15.87	28.59 (1.18)	42.94 (3.26)	1.43	1.38
EMAC	23.83	14.75	29.77 (0.88)	45.57 (1.93)	1.37	1.45
GISS-E2-2-G*	20.56	11.46	32.23 (1.87)	37.06 (3.50)	1.42	1.31
LMDz6*	11.30	9.81	37.01 (2.20)	32.47 (1.69)	1.55	1.41
MIROC-AGCM-LL	23.48	19.26	30.31 (0.78)	30.90 (1.11)	1.46	1.49
MIROC-ESM	27.77	18.15	27.96 (0.57)	29.90 (1.15)	1.38	1.34
MRI-ESM2.0	21.53	16.70	35.02 (1.39)	39.35 (1.88)	1.43	1.40
WACCM5-110L	26.00	16.87	27.13 (0.77)	36.99 (1.31)	1.40	1.49

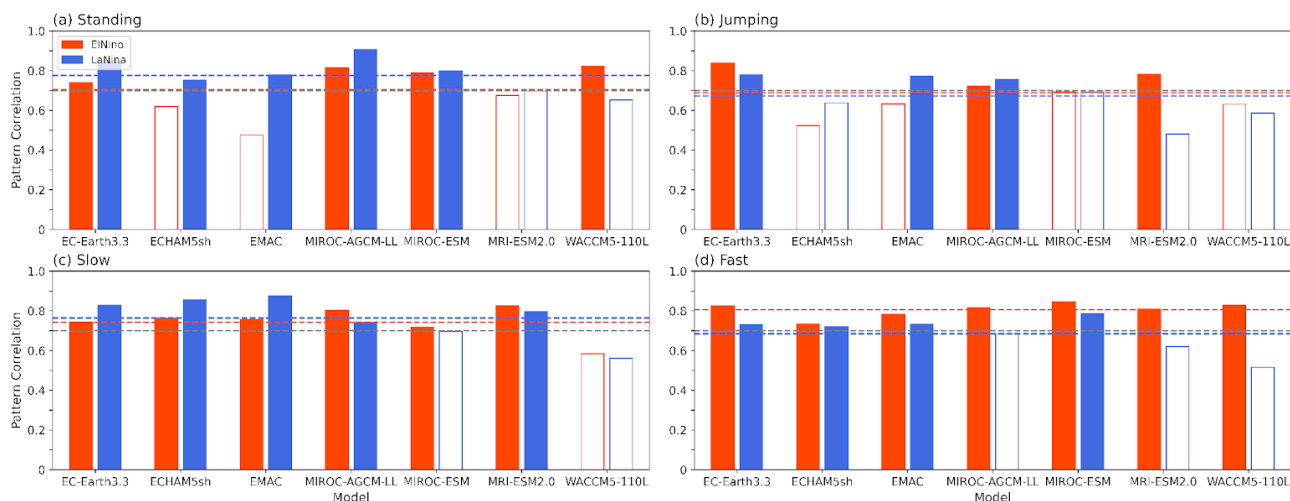
397  
 398 Based on ERA5, La Niña events are roughly nine days longer than El Niño events on average. Wei and Ren (2019) found La  
 399 Niña to support both high-frequency (lifetime ~40 days) and low frequency (lifetime ~80 days) MJOs, which conceivably  
 400 explains the much larger ERA5 lifetime standard errors during La Niña compared with El Niño. Strikingly, the difference in  
 401 lifetime and its standard error between ENSO phases is nearly ubiquitous across the models. With the exception of LMDZ6,  
 402 La Niña lifetimes are between 0.59 (MIROC-AGCM-LL) and 15.8 (EMAC) days longer than El Niño lifetimes. Models in  
 403 similar families, for instance ECHAM5sh and EMAC as well as MIROC-AGCM-LL and MIROC-ESM, typically have similar



404 magnitude differences in their Pohl and Matthews (2007) statistics between ENSO phases. All models simulate more MJO  
 405 events during El Niño, which is consistent with ERA5, however the difference in the number of events between ENSO phases  
 406 is generally larger in the models than in ERA5. MJO amplitude is only marginally larger during La Niña based on ERA5  
 407 whereas six of the nine models have larger amplitudes during El Niño.

408  
 409 Analyzing MJO diversity can provide further insight into its speed and propagation. K-means clustering of MJO convection  
 410 tracks from empirical OLR Hovmöller diagrams reveal four major MJO propagation archetypes: standing, jumping, slow  
 411 propagating, and fast propagating events (Wang et al. 2019). Composites of the background SSTs associated with these  
 412 archetypes show standing MJOs to be concurrent with La Niña, fast MJOs overlap with El Niño, and jumping and slow  
 413 events have no clear association with either ENSO phase. The experimental setup here enables us to test if in fact some of the  
 414 MJO archetypes predominate given a background ENSO forcing. Note that fast and slow events can occur during either ENSO  
 415 phase and so there is at least some sensitivity of the previous results to sampling variability (Yadav and Straus 2017).

416  
 417



418  
 419 **Figure 5: Pattern correlations between the ERA5 and simulated time-longitude (Hovmöller) 10°S-10°N convective OLR anomaly**  
 420 **composites (OLR < -5 W/m<sup>2</sup>) corresponding to each of the four K-means clusters MJO archetypes defined in Wang et al. (2019).**  
 421 **Multi-model average El Niño and La Niña correlations are shown by red and blue dashed lines, respectively, and shaded (non-**  
 422 **shaded) bars exceed (fall beneath) these multi-model means. The gray dashed line marked at a correlation of 0.7 is a heuristic**  
 423 **threshold used here and elsewhere (Back et al. 2024) to decide when a particular model’s MJO archetype is well captured by a**  
 424 **model.**

425  
 426 To gauge how similar the model archetypes are to those in reanalysis, pattern correlations are calculated between the ERA5  
 427 and model time-longitude tropical OLR convective anomaly composites corresponding to a given cluster. This measures how  
 428 well the models represent the various observed MJO archetypes and helps to assess whether or not the representation of a  
 429 given archetype improves in the presence of either ENSO forcing. Offline multi-model assessments of MJO diversity (Back  
 430 et al. 2024) have revealed that a pattern correlation of 0.7 is a reasonable threshold to distinguish between good and poorly

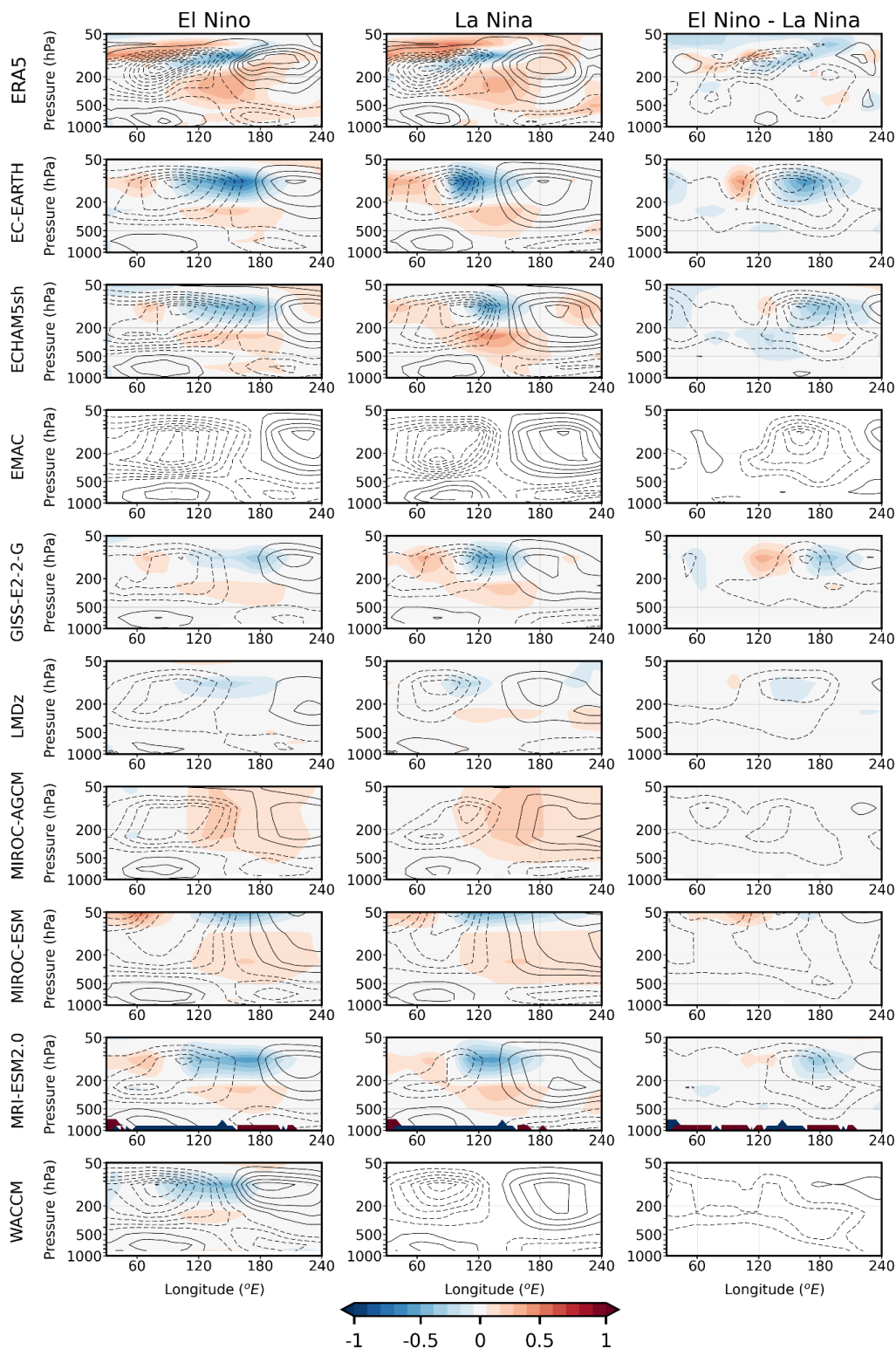


431 simulated OLR Hovmöllers. For the standing MJO (Fig. 5a), five of the 14 models have correlations below 0.7, hence we  
432 shade their bar white. Although the representation of the standing cluster is poor in roughly a third of the simulations, the  
433 representation of the standing MJO is notably better during La Niña, with the multi-model pattern correlation exceeding its El  
434 Niño equivalent by 0.09. The pattern correlation between the observed and simulated jumping MJOs falls beneath 0.7 for over  
435 half of the simulations, indicating that the models really struggle to represent this archetype (Fig. 5b). However, jumping MJOs  
436 are not currently thought to be influenced by ENSO and so are not considered further. Observations indicate that slowly  
437 propagating MJOs are typically concurrent with La Niña, however the associated SST pattern is weak and not statistically  
438 significant (Wang et al. 2019; Back et al. 2024). Similarly, we find the representation of slowly propagating MJOs to be slightly  
439 better amongst the La Niña simulations, but likely statistically indistinguishable from the El Niño correlations (Fig. 5c). In  
440 stark contrast, for fast events, every model's El Niño simulation represents this archetype better than the La Niña equivalent,  
441 culminating in the El Niño multi-model mean correlation exceeding the La Niña mean by 0.11 (Fig. 5d). In summary, the  
442 diversity analysis affirms that the fast and standing MJO archetypes are closely associated with El Niño and La Niña,  
443 respectively.

444

445 The vertical structure of the MJO differs between slow and fast propagating events (Wang et al. 2019). To consider this further,  
446 we regress the latitudinally averaged 10°S-10°N zonal wind and temperature from ERA5 and the models onto their phase 3/4  
447 RMM indices as in Hendon and Abhik (2018) and form pressure-longitude cross-sections (Figure 6). Phases 3/4, when the  
448 MJO convection is over the western Maritime Continent, are of interest because ENSO modulates the low-frequency  
449 circulation here through its effect on the Walker Circulation, giving it a pathway to influence MJO propagation (Sun et al.  
450 2019; Suematsu and Miura 2022). Irrespective of the ENSO phase, the MJO in ERA5 exhibits a quadrupole structure in zonal  
451 wind, all of which is centered around a tropospheric warming at 140°E that peaks in amplitude near 300 hPa (cf. Jiang et al.  
452 2015).

453







455 **Figure 6: Pressure-longitude cross-sections of the 10°S-10°N zonal wind and temperature regressed onto the Phase 3/4 RMMs as in**  
456 **Hendon and Abhik (2018). Black contours show zonal wind (intervals of +/- 0.5, 1.5, 2.5 m/s...) and temperature is shaded between**  
457 **-1 and 1 °C. EMAC is missing temperature and WACCM's La Nina temperature includes a conspicuous artifact that we are still**  
458 **looking into.**

459  
460 Although the ERA5 El Niño and La Niña composites are similar overall, subtracting the two reveals that they differ due to the  
461 El Niño composite including a stronger Kelvin wave (cf. Fig. 2). The characteristic features of the wave include its cold cap  
462 temperature anomaly in the UTLS, which is in quadrature with easterly zonal wind anomalies, all of which tilt eastward with  
463 increasing height above ~200 hPa and westward with increasing height below (Straub and Kiladis 2002; Kim et al. 2013; Yuni  
464 et al. 2019; Nakamura and Takayabu 2022). Judging by the longitude of the ERA5 100 hPa cold cap maximas, the Kelvin  
465 wave embedded in the composite El Niño MJO is shifted further east compared to its La Niña equivalent, evidence that it is  
466 propagating faster. This corresponds to the alignment of ERA5 Kelvin wave spectral power along the deepest equivalent depth  
467 dispersion curves during El Niño in Fig. 2.

468  
469 Consistent with recent studies, the surface easterlies positioned east of the MJO convection are indeed stronger during El Niño  
470 in reanalysis (Wang et al. 2019; Wei and Ren 2019). We attribute the amplification of these easterlies to the Kelvin wave's  
471 planetary scale signature in wind, which better bridges the MJO lower tropospheric easterlies over the Pacific with the upper  
472 tropospheric easterly outflow over the Indian Ocean; compare the 500 hPa zonal winds at 150°E between El Niño and La Niña.  
473 This enhanced continuity of the MJO easterlies during El Niño is a robust feature amongst the models and is particularly clear  
474 in the El Niño minus La Niña composites of EC-EARTH3.3, ECHAM5sh, MIROC-AGCM-LL, MIROC-ESM and MRI-  
475 ESM2.0. The models, however, struggle to represent the detailed temperature structure of the Kelvin wave and they exhibit  
476 MJO temperature anomalies that can differ significantly from ERA5 (e.g., MIROC family).

477  
478 The vertical structure of the MJO zonal wind anomalies is more baroclinic during La Niña. This may be attributed to a weaker  
479 and slower propagating Kelvin wave during La Niña. However, it is also possible that the amplification of the equatorial  
480 Rossby wave during La Niña (cf. Figure 2) projects onto the MJO's vertical structure. For instance, similar to the western  
481 portion of the phase 3/4 MJO winds, these waves (when located in the eastern hemisphere) have a first baroclinic structure in  
482 zonal wind that consists of low-level westerlies and upper-level easterlies (Kiladis et al. 2009; Yuni et al. 2019; Nakamura and  
483 Takayabu 2022). Following from the robust amplification of the equatorial Rossby wave across the models during La Niña, it  
484 was hypothesized that the low-level westerlies west of the MJO convection would be stronger during La Niña than El Niño  
485 like in Wei and Ren (2019). This does not appear to be the case though and no first baroclinic zonal wind structure stands out  
486 in the El Niño minus La Niña composites. The signal of the equatorial Rossby wave does, however, appear to be visible in the  
487 temperature field. These waves are associated with a mid to upper tropospheric warming that is centered around 300 hPa  
488 (Kiladis et al. 2009, Fig. 18c). This region of the upper troposphere is warmer in all of the La Niña simulations, with the  
489 exception of MIROC-ESM in which the warming is marginally stronger in the El Niño composite.





490 **3.2 The lack of QBO-MJO coupling**

491 The results in the previous section indicate that ENSO modulates the MJO’s propagation, promoting faster MJOs during El  
 492 Niño and the opposite during La Niña. However, it is possible that aliased signals from the spontaneously generated QBOs are  
 493 embedded in the aforementioned results. Therefore, in this section we look for evidence of QBO-MJO coupling. As a first  
 494 step, the representation of the QBO is documented using previously defined metrics, with a specific interest in quantifying the  
 495 “lowest level” that the QBO descends to in the lower stratosphere. Insufficient descent is a known bias, which may hinder the  
 496 QBO from modulating other potentially important variables near the tropopause such as temperature (Richter et al. 2020; Kim  
 497 et al. 2020). Similar to Schenzinger et al. (2017), the lowest level that QBO reaches is found by averaging the QBO Fourier  
 498 amplitude (see Methods) over 5°S-5°N, identifying the maximum amplitude (fixed at 20 hPa here), and then finding the isobar  
 499 in the lower stratosphere where the amplitude equals 10% of the maximum.

500

501 *Table 3: From left to right, QBO easterly, westerly, and total amplitude, the lowest level that the QBO descends to, its vertical extent, and*  
 502 *its latitudinal extent. These statistics are computed using the same “QBO cycles” (see Methods) and QBO periodicity statistics that are*  
 503 *reported in Kawatani et al. (2024, in preparation). Vertical extents listed as “N/A” were missing data at middle stratospheric isobars, which*  
 504 *prevents the calculation. ECHAM5sh’s El Niño simulation QBO Fourier amplitude is split into two parts above and below ~10 hPa (not*  
 505 *shown), which is why its vertical extent is only 10.4 km.*

506

	EN easterly amplitude (m/s)	LN easterly amplitude (m/s)	EN westerly amplitude (m/s)	LN westerly amplitude (m/s)	EN QBO amplitude (m/s)	LN QBO amplitude (m/s)	EN lowest level (hPa)	LN lowest level (hPa)	EN vertical extent (km)	LN vertical extent (km)	EN latitudinal extent (degrees lat.)	LN latitudinal extent (degrees lat.)
EC- EARTH3.3	-15.5	-15.6	16	16.7	15.8	16.2	70.4	67.5	17.5	15.6	21.4	20.8
ECHAM5sh	-16.2	-24.4	17.4	21.8	16.8	23.1	64.6	70.3	10.4	20.2	21	21.5
EMAC	-22.3	-24	21.2	17.8	21.8	20.9	66.2	64.7	19	21.2	21.2	21.9
LMDz6	-16.7	-16.1	19.1	14.3	17.9	15.2	68.1	54.3	N/A	N/A	17.7	16.9
GISS-E2-E- G	-24.3	-18.9	23.1	16.6	23.7	17.8	74.7	59.7	19.9	14	20.5	19.4
MIROC- AGCM-LL	-15.4	-16.4	14.8	15.3	15.1	15.8	68.1	66.9	N/A	N/A	20.3	21.1
MIROC- ESM	-18.4	-18.5	16.9	17.5	17.6	18	66.2	68.9	20.5	24.9	19.9	20.2
MRI- ESM2.0	-20.6	-21.7	24.6	24.4	22.6	23	82.4	82.8	17.7	17.3	19.5	20.5



WACCM5-110L	-23.4	-23.4	24	24	23.7	23.7	69.5	87	17.6	18.5	19.7	21.4
ERA5	-24.1		24.5		24.3		92.2		18.1		23.9	

507

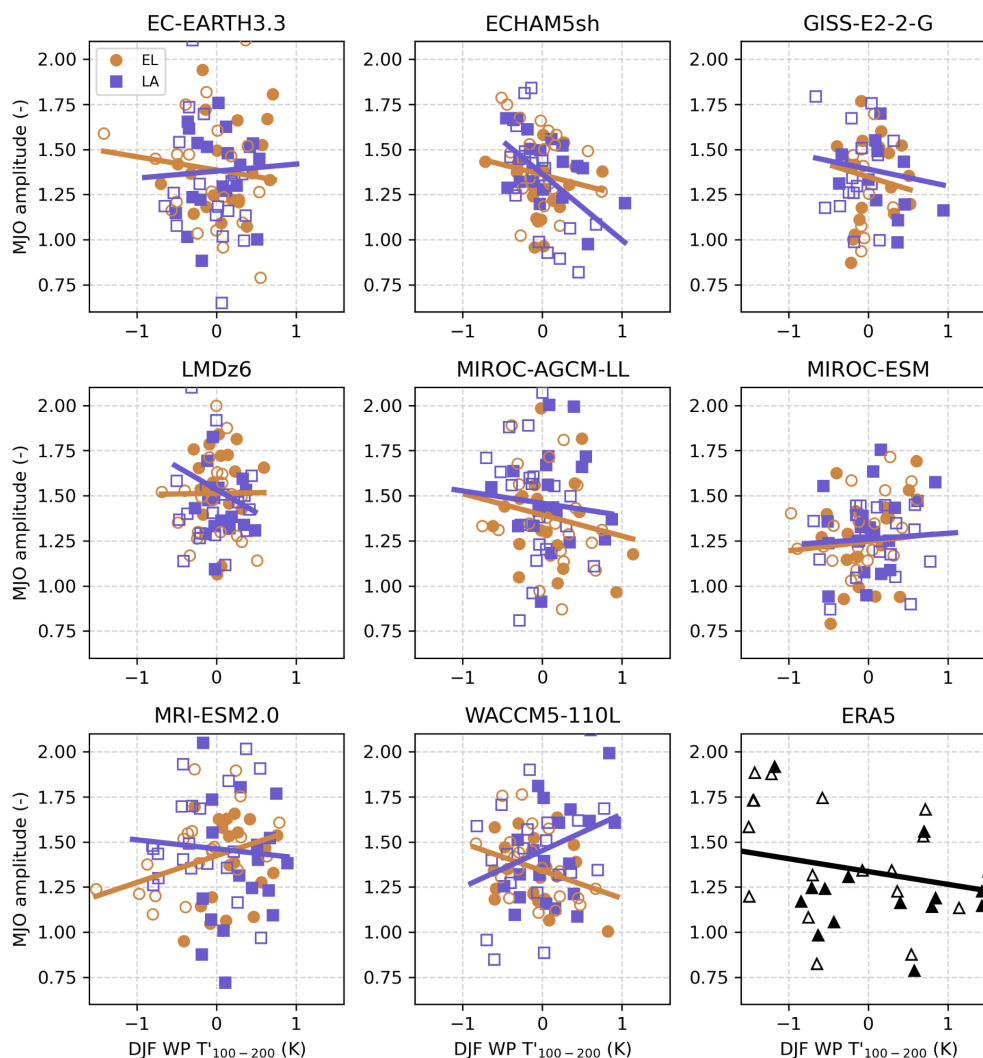
508 The QBO descends to 92.2 hPa in ERA5 (Table 3). Of the simulated QBOs, the majority do not reach beneath 70 hPa,  
 509 indicating that they are likely too high in altitude to influence the tropical atmosphere beneath 100 hPa as observed (Tegtmeier  
 510 et al. 2020). One outlier is the WACCM5-110L’s La Niña simulation whose lowest isobar of 87 hPa is fairly similar to the  
 511 ERA5 benchmark. Nonetheless, sensitivity tests with this simulation in which MJO amplitude is computed as a function of  
 512 lower stratospheric QBO phase reveals its MJO to be insensitive to the QBO in the observed way (not shown). ENSO phase  
 513 does not have consistent effects on what lowest isobar a given model’s QBO reaches. For example, GISS-E2-E-G and LMDz6  
 514 favor much stronger descent of the QBO into the lower stratosphere during El Niño whereas WACCM5-110L’s ENSO  
 515 simulations reflect a strong opposite signed response.

516

517 In general, the metrics do not change systematically by ENSO phase. For example, QBO amplitude is stronger during La Niña  
 518 in five of the nine models. El Niño and La Niña QBO amplitudes differ by less than 1 m/s for all models except ECHAM5sh,  
 519 GISS-E2-EG, and LMDz6. ECHAM5sh favors a stronger QBO amplitude during La Niña, owing to intensified QBO easterlies  
 520 and westerlies during this ENSO phase. Conversely, GISS-E2-EG, and LMDz6 favor stronger easterly, westerly, and total  
 521 QBO amplitudes during El Niño. Of the 12 simulations corresponding to the six other models, EC-EARTH3.3, EMAC,  
 522 MIROC-AGCM-LL, MIROC-ESM, MRI-ESM2.0, and WACCM5-110L, the magnitude of their easterly and westerly QBO  
 523 amplitudes is stronger during La Niña in eight of the 12 simulations. The effect of ENSO phase on vertical extent is inconsistent  
 524 across the models and difficult to evaluate entirely because of missing data in two models and an unrealistic QBO Fourier  
 525 amplitude structure in ECHAM5sh’s El Niño simulation. Although the models ubiquitously underestimate the latitudinal  
 526 extent of the QBOs relative to ERA5, it may be noteworthy that six of nine models have wider QBO latitudinal extents during  
 527 La Niña. The boreal winter polar stratospheric wind response to the QBO is stronger when the QBO is wider (Hansen et al.  
 528 2013) and there is a preference for this teleconnection to happen during La Niña over the observed record (Kumar et al. 2022).

529

530



531  
532 **Figure 7: Scatter plot of warm-pool averaged (10°S-10°N, 45°E-180°E) tropopause stability anomalies (100 hPa minus 200 hPa**  
533 **temperature) versus December-February MJO amplitude. Lines represent the slope of the regression line during El Niño (orange**  
534 **or La Niña (purple). Easterly and westerly QBO phases, which are delineated by the sign of the December-February 5°S-5°N 50 hPa**  
535 **zonal mean zonal-wind, are denoted by open and filled markers, respectively.**  
536

537 While the aforementioned QBO metrics help to broadly characterize the form of each model's QBO, they are non-time-varying  
538 quantities and have less value for better understanding seasonal phenomena such as the predominantly boreal winter QBO-  
539 MJO interaction. To incorporate the effects of seasonality, scatterplots of December-February warm-pool averaged tropopause  
540 stability versus December-February MJO amplitude are made as a function of QBO phase for each of the simulations  
541 (Klotzbach et al. 2019). MJO amplitude is expected to increase as tropopause stability decreases (Son et al. 2017; Klotzbach  
542 et al. 2019), as is apparent based on ERA5 (Fig. 7). This metric is relevant for considering QBO-MJO coupling because the  
543 QBO's effect on lower stratospheric stability (e.g., Densmore et al. 2019) is one of the suspected physical mechanisms coupling



544 the QBO and MJO. In general, the models do not reproduce the observed inverse relation between MJO amplitude and 100-  
545 200 hPa stability and stratifying the results either by ENSO phase or QBO phase does not change this. The linear response of  
546 the MJO amplitude to the tropopause stability, which is negative in observations, does not change consistently with the ENSO  
547 phase. It is worth noting that the mean DJF stability in the models is generally close to that of ERA5 (-28.7 K) except for the  
548 GISS model, which showcases a smaller gradient (-23.3 K), and all models appear to underestimate its interannual variability,  
549 as evident by the smaller range compared to ERA5. Furthermore, the stratification by QBO phase (with eQBO associated with  
550 lower stability values, and vice versa for the wQBO) is also small or absent in models, possibly due to a limited influence of  
551 the QBO at tropopause heights (Serva et al., 2022). Further sensitivity tests were done to see if the model QBOs simulate a  
552 QBO-MJO amplitude relationship when the MJO is in a particular phase (e.g., Lim and Son 2020; Lawrence et al. 2023); no  
553 systematic effect was detected (not shown).



MJO Activity (OLR  $\sigma$ )

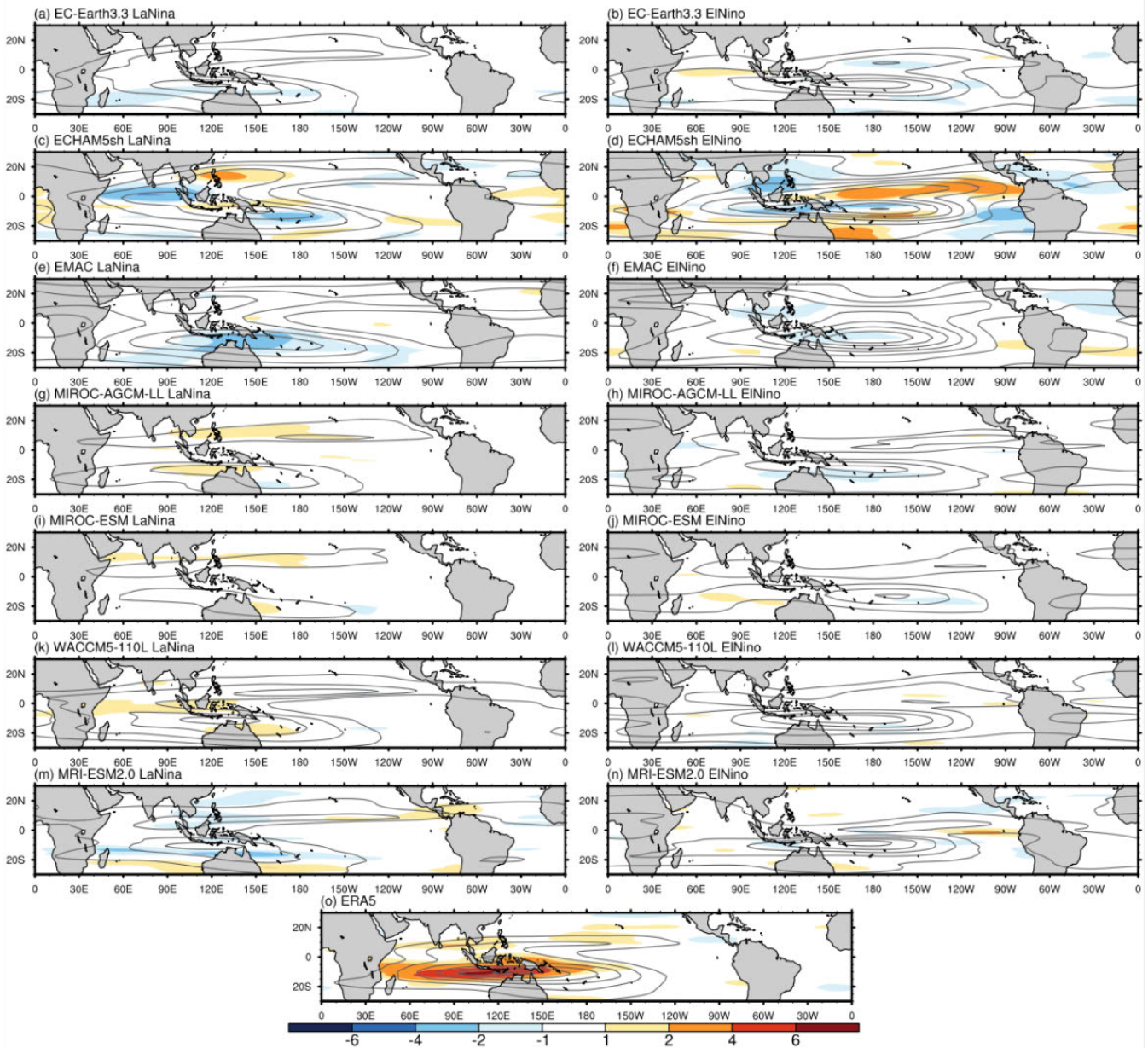


**Figure 8:** Gray contours show the MJO activity defined as the standard deviation of MJO-filtered OLR for each model and ENSO phase, as well as for ERA5 (6n). The color-filled contours show the MJO-QBO relationship as the difference in MJO activity for the eastward minus westward QBO phases for each model and ERA5.

To further evaluate the representation of QBO-MJO coupling in the models, Figure 8 presents the effect of QBO phase on MJO activity (see Methods). As shown in previous studies (e.g., Kim et al. 2020), the models do not capture the observed QBO-MJO relationship, which has maximum signal over the maritime continent region (Fig. 8m) illustrating the enhancement





562 of MJO activity during easterly QBO phase. With La Niña forcing, MIROC-AGCM-LL and WACCM5-110L show a weak  
563 positive signal over the Maritime Continent (Fig. 8g, k), however EC-EARTH3.3, ECHAM5sh, and EMAC exhibit rather  
564 different responses. No change in the MJO activity by QBO phase is evident in the El Niño simulations either. There is,  
565 however, a clear eastward shift of the MJO activity towards the Pacific during El Niño, corroborating the observational work  
566 of Kessler (2001) and the climate model based study of Tam and Lau (2005).

#### 567 **4 Discussion and conclusions**

568 The observed interannual variability of the MJO is influenced by multiple parts of the climate system. Due to their impact on  
569 the tropical troposphere and prominent fluctuations at interannual timescales, ENSO and the QBO are known drivers of the  
570 MJO's year to year variability, however it is difficult to definitively isolate their influence on the MJO because of how short  
571 and noisy the observational record is (Randall et al. 2023). Building on previous work, we have analyzed the representation of  
572 the MJO in nine climate models that are forced by prescribed perpetual El Niño and La Niña conditions and which include  
573 spontaneously generated QBOs. Although the models exhibit difficulties simulating the MJO, several previously reported  
574 effects of the ENSO phase on the MJO are corroborated by this coordinated set of experiments. These include faster  
575 propagation of the MJO during El Niño versus slower propagation during La Niña, manifesting as shorter and longer lifetimes,  
576 respectively, stronger amplitude of the MJO during El Niño, and east-west shifting of the MJO timescale variance towards the  
577 east Pacific during El Niño and towards the west Pacific and Indian Ocean during La Niña. As in the observational record, it  
578 is possible that aliasing from the QBO is superimposed on what are thought to be MJO changes due to ENSO. However, we  
579 find that the climate models considered here include nearly no evidence of QBO-MJO coupling. While this hampers further  
580 understanding of the mechanisms responsible for coupling the QBO and MJO, in all likelihood this eliminates the QBO as a  
581 driver of the MJO in this set of experiments, which increases our confidence that the aforementioned changes in the MJO are  
582 arising due to ENSO. Experiments with specified rather than internally generated QBOs can help understanding the processes  
583 at play, which remain elusive (Martin et al., 2023).

584  
585 These results highlight that the interannual variability of the MJO is sensitive to ENSO in several regards, in contrast with  
586 Slingo et al. (1999) and Hendon et al. (1999). These studies reported a weak simultaneous relationship between ENSO and  
587 MJO activity. Hendon et al. (1999) clarified that increased MJO activity coincides with an increased number of MJO events  
588 and enhanced intraseasonal convective activity around the Maritime Continent. While these attributes of the MJO were largely  
589 insensitive to SSTs in their study, the models here unambiguously simulate more events during El Niño (Table 2), which are  
590 of stronger MJO activity than their La Niña equivalents (Figure 8). We suspect that the distinction between our results and the  
591 aforementioned studies is related to the timescale over which the oceanic component of ENSO modulates the atmosphere.  
592 Recent studies show that while the likelihood of MJO occurrence and its propagation speed are only weakly correlated with  
593 tropical intraseasonally filtered SSTs (agreeing with the aforementioned studies), they are strongly correlated with low-





594 frequency (e.g., > 90 days) SSTs (Suematsu and Miura 2018; 2022). Along the same lines, Newman et al. (2009) found air-  
595 sea coupling to have weak effects on subseasonal atmospheric variability, but strong influence on the long-term atmospheric  
596 circulation. In light of this and our use of a simplified climate system in which smoothed monthly SSTs are prescribed,  
597 intraseasonal and interannual SST fluctuations are explicitly ignored, and the downward impact of the MJO on intraseasonal  
598 SSTs (Zhang and Gottschalk 2002; Hendon et al. 2007; Newman et al. 2009) is not simulated, we deduce that the different  
599 basic state circulations set up by the indefinite ENSO forcings enables distinct MJOs. This interpretation of the low-frequency  
600 SSTs as an important modulator of the MJO aligns with studies which have attributed variability in the MJO's propagation to  
601 ENSO (Wei and Ren 2019; Wang et al. 2019; Dasgupta et al. 2021; Back et al. 2024) as well as studies employing climate  
602 models in which MJO propagation can be modulated by changing the horizontal gradients of the background SST field (Kang  
603 et al. 2013; Jiang et al. 2020).

604  
605 Compared with the La Niña simulations, all El Niño simulations include amplified Kelvin waves whereas equatorial Rossby  
606 waves intensify in the presence of perpetual La Niña conditions. Consistent with the reported relationship between these waves  
607 and the MJO, all models simulate faster MJO propagation in their El Niño simulation. This is further supported by the MJO  
608 diversity analysis, which reveals that models simulate the fast and standing MJO archetypes well in the presence of perpetual  
609 El Niño and La Niña conditions, respectively. In addition, the MJO's phase 3/4 vertical structures highlight that lower  
610 tropospheric easterlies do intensify to the east of the MJO's major convection during El Niño across most models, which we  
611 interpret to result from the intensification of the Kelvin wave.

612  
613 While the relationship between Kelvin waves, equatorial Rossby waves, and ENSO is well established by previous studies  
614 employing empirical data and reanalysis, this is the first time, to the best of our knowledge, that this relationship has been  
615 ubiquitously affirmed by a coordinated set of climate model experiments with prescribed ENSO forcings. The robustness of  
616 this result across models suggests that it is worthwhile considering how these wave responses to ENSO influence other parts  
617 of the climate system. For instance, Kelvin waves are a source of resolved wave forcing for the QBO (Baldwin et al. 2001;  
618 Taguchi 2010; Pahlavan et al. 2021) and more rapid descent of the QBO's westerly shear zones during El Niño in observations  
619 has been attributed to their intensification (Das and Pan 2016). The periodicity of the QBO in the El Niño simulations is in  
620 fact shorter than in the La Niña simulations across all models considered here (Kawatani et al., in preparation), however, the  
621 extent to which Kelvin waves are responsible for this as opposed to other waves (e.g., Kawatani et al. 2019), is yet to be  
622 quantified across all of the models. The convectively coupled wave responses presented here may also be relevant for better  
623 understanding ENSO diversity. El Niño events vary in type and intensity due to the influence of westerly wind bursts, which  
624 introduce asymmetry and irregularity into ENSO's phase changes (Chen et al. 2015). Westerly wind bursts are more frequent  
625 during the convective phases of equatorial Rossby waves and the MJO, especially strong MJOs (Puy et al. 2016). Hence, the  
626 atmospheric responses to ENSO, such as the amplifications of the MJO during El Niño (Figs. 2-4) and of the convectively  
627 coupled Rossby wave during La Niña, have a pathway to influence ENSO's oceanic component.



628

629 **Code availability**

630

631 The code used for the wavenumber-frequency analysis is publicly available through the National Center for Atmospheric  
632 Research (NCAR) Command Language (NCL): <https://www.ncl.ucar.edu/Applications/mjoelivar.shtml>. A reproduction of  
633 NCL's Wheeler-Kiladis (1999) routine in Python is available here: [https://github.com/brianpm/wavenumber\\_frequency](https://github.com/brianpm/wavenumber_frequency).  
634 Python code, which assesses QBO morphology is available here: [https://github.com/NOAA-GFDL/MDTF-](https://github.com/NOAA-GFDL/MDTF-diagnostics/blob/main/diagnostics/stc_qboenso/stc_qboenso.py)  
635 [diagnostics/blob/main/diagnostics/stc\\_qboenso/stc\\_qboenso.py](https://github.com/NOAA-GFDL/MDTF-diagnostics/blob/main/diagnostics/stc_qboenso/stc_qboenso.py).

636

637 **Data availability**

638 Storage for the QBOi multi-model data set is provided by the Centre for Environmental Data Analysis (CEDA) whose data  
639 and processing service is called JASMIN. Interested users must obtain a JASMIN login account and take the necessary steps  
640 to access the QBOi group workspace within JASMIN, which contains the perpetual ENSO simulations. Certain derived model  
641 products (e.g., the MJO RMMs) may be made available upon request.

642

643 **Author contributions**

644 DE, FS, JC, SYB, CO, and JR contributed to the conceptualization of this study. DE, FS, JC, and SYB performed the data  
645 analyses and produced the figures and tables. All authors contributed to the review and editing of this manuscript.

646

647 **Competing interests**

648 The authors declare that they have no conflict of interest.

649

650 **Acknowledgements**

651 DE was supported in part by NOAA Cooperative Agreement NA22OAR4320151 and appreciates helpful discussions with  
652 John Albers, Juliana Dias, George Kiladis, Matthew Newman, and Brandon Wolding. The ECHAM5sh simulations were  
653 performed thanks to an ECMWF Special Project awarded to FS. YK[KY1] was supported by JSPS KAKENHI (JP22K18743)  
654 and the Environment Research and Technology Development Fund (JPMEERF20242001) of the Environmental Restoration  
655 and Conservation Agency provided by Ministry of the Environment of Japan. YK and SW were supported by JSPS KAKENHI  
656 (JP22H01303 and JP23K22574). SW was supported by MEXT-Program for the advanced studies of climate change projection  
657 (SENTAN) Grant Number JPMXD0722681344. The numerical simulations of MIROC models were performed using the Earth  
658 Simulator. The GFD-DENNOU Library and GrADS were used to draw the figures. TK and SV acknowledge support by the  
659 state of Baden-Württemberg through bwHPC. Portions of this work were supported by the National Center for Atmospheric  
660 Research (NCAR), which is a major facility sponsored by the National Science Foundation (NSF) under Cooperative  
661 Agreement 1852977. Portions of this study were supported by the Regional and Global Model Analysis (RGMA) component



662 of the Earth and Environmental System Modeling Program of the U.S. Department of Energy's Office of Biological and  
663 Environmental Research (BER) via NSF Interagency Agreement 1844590. The authors gratefully acknowledge the UK Centre  
664 for Environmental Data Analysis for providing resourcing for the multimodel dataset.

665

## 666 References

667

668 Ahn, M.-S., Kim, D., Sperber, K. R., Kang, I.-S., Maloney, E., Waliser, D., and Hendon, H.: MJO simulation in CMIP5 climate  
669 models: MJO skill metrics and process-oriented diagnosis, *Clim Dyn*, 49, 4023–4045, [https://doi.org/10.1007/s00382-017-](https://doi.org/10.1007/s00382-017-3558-4)  
670 [3558-4](https://doi.org/10.1007/s00382-017-3558-4), 2017.

671

672 Ahn, M., Kim, D., Kang, D., Lee, J., Sperber, K. R., Gleckler, P. J., Jiang, X., Ham, Y., and Kim, H.: MJO Propagation Across  
673 the Maritime Continent: Are CMIP6 Models Better Than CMIP5 Models?, *Geophysical Research Letters*, 47,  
674 e2020GL087250, <https://doi.org/10.1029/2020GL087250>, 2020.

675

676 Back, S.-Y., Kim, D., and Son, S.-W.: MJO Diversity in CMIP6 Models, *Journal of Climate*, 37, 4835–4850,  
677 <https://doi.org/10.1175/JCLI-D-23-0656.1>, 2024.

678

679 Baldwin, M. P., Gray, L. J., Dunkerton, T. J., Hamilton, K., Haynes, P. H., Randel, W. J., Holton, J. R., Alexander, M. J.,  
680 Hirota, I., Horinouchi, T., Jones, D. B. A., Kinnnersley, J. S., Marquardt, C., Sato, K., and Takahashi, M.: The quasi-biennial  
681 oscillation, *Reviews of Geophysics*, 39, 179–229, <https://doi.org/10.1029/1999RG000073>, 2001.

682

683 Bechtold, P., Semane, N., Lopez, P., Chaboureau, J.-P., Beljaars, A., and Bormann, N.: Representing Equilibrium and  
684 Nonequilibrium Convection in Large-Scale Models, *Journal of the Atmospheric Sciences*, 71, 734–753,  
685 <https://doi.org/10.1175/JAS-D-13-0163.1>, 2014.

686

687 Berrington, A. H., Sakaeda, N., Dias, J., and Kiladis, G. N.: Relationships Between the Eastward Propagation of the Madden-  
688 Julian Oscillation and Its Circulation Structure, *JGR Atmospheres*, 127, e2021JD035806,  
689 <https://doi.org/10.1029/2021JD035806>, 2022.

690

691 Bushell, A. C., Anstey, J. A., Butchart, N., Kawatani, Y., Osprey, S. M., Richter, J. H., Serva, F., Braesicke, P., Cagnazzo, C.,  
692 Chen, C.-C., Chun, H.-Y., Garcia, R. R., Gray, L. J., Hamilton, K., Kerzenmacher, T., Kim, Y.-H., Lott, F., McLandress, C.,  
693 Naoe, H., Scinocca, J., Smith, A. K., Stockdale, T. N., Versick, S., Watanabe, S., Yoshida, K., and Yukimoto, S.: Evaluation  
694 of the Quasi-Biennial Oscillation in global climate models for the SPARC QBO-initiative, *Quart J Royal Meteorol Soc*, 148,  
695 1459–1489, <https://doi.org/10.1002/qj.3765>, 2022.

696

697 Butchart, N., Anstey, J. A., Hamilton, K., Osprey, S., McLandress, C., Bushell, A. C., Kawatani, Y., Kim, Y.-H., Lott, F.,  
698 Scinocca, J., Stockdale, T. N., Andrews, M., Bellprat, O., Braesicke, P., Cagnazzo, C., Chen, C.-C., Chun, H.-Y., Dobrynin,  
699 M., Garcia, R. R., Garcia-Serrano, J., Gray, L. J., Holt, L., Kerzenmacher, T., Naoe, H., Pohlmann, H., Richter, J. H., Scaife,  
700 A. A., Schenzinger, V., Serva, F., Versick, S., Watanabe, S., Yoshida, K., and Yukimoto, S.: Overview of experiment design  
701 and comparison of models participating in phase 1 of the SPARC Quasi-Biennial Oscillation initiative (QBOi), *Geosci. Model*  
702 *Dev.*, 11, 1009–1032, <https://doi.org/10.5194/gmd-11-1009-2018>, 2018.

703

704 Chen, D., Lian, T., Fu, C., Cane, M. A., Tang, Y., Murtugudde, R., Song, X., Wu, Q., and Zhou, L.: Strong influence of  
705 westerly wind bursts on El Niño diversity, *Nature Geosci*, 8, 339–345, <https://doi.org/10.1038/ngeo2399>, 2015.

706



- 707 Chikira, M. and Sugiyama, M.: A Cumulus Parameterization with State-Dependent Entrainment Rate. Part I: Description and  
708 Sensitivity to Temperature and Humidity Profiles, *Journal of the Atmospheric Sciences*, 67, 2171–2193,  
709 <https://doi.org/10.1175/2010JAS3316.1>, 2010.
- 710  
711 Das, U. and Pan, C. J.: Equatorial atmospheric Kelvin waves during El Niño episodes and their effect on stratospheric QBO,  
712 *Science of The Total Environment*, 544, 908–918, <https://doi.org/10.1016/j.scitotenv.2015.12.009>, 2016.
- 713  
714 Dasgupta, P., Roxy, M. K., Chattopadhyay, R., Naidu, C. V., and Metya, A.: Interannual variability of the frequency of MJO  
715 phases and its association with two types of ENSO, *Sci Rep*, 11, 11541, <https://doi.org/10.1038/s41598-021-91060-2>, 2021.
- 716  
717 Densmore, C. R., Sanabia, E. R., and Barrett, B. S.: QBO Influence on MJO Amplitude over the Maritime Continent: Physical  
718 Mechanisms and Seasonality, *Monthly Weather Review*, 147, 389–406, <https://doi.org/10.1175/MWR-D-18-0158.1>, 2019.
- 719  
720 Emanuel, K. A.: A Scheme for Representing Cumulus Convection in Large-Scale Models, *J. Atmos. Sci.*, 48, 2313–2329,  
721 [https://doi.org/10.1175/1520-0469\(1991\)048<2313:ASFRCC>2.0.CO;2](https://doi.org/10.1175/1520-0469(1991)048<2313:ASFRCC>2.0.CO;2), 1991.
- 722  
723 Emori, S., Nozawa, T., Numaguti, A., and Uno, I.: Importance of Cumulus Parameterization for Precipitation Simulation over  
724 East Asia in June., *Journal of the Meteorological Society of Japan*, 79, 939–947, <https://doi.org/10.2151/jmsj.79.939>, 2001.
- 725  
726 Fernandes, L. G. and Grimm, A. M.: ENSO Modulation of Global MJO and Its Impacts on South America, *Journal of Climate*,  
727 36, 7715–7738, <https://doi.org/10.1175/JCLI-D-22-0781.1>, 2023.
- 728 Hendon, H. H. and Abhik, S.: Differences in Vertical Structure of the Madden-Julian Oscillation Associated With the Quasi-  
729 Biennial Oscillation, *Geophysical Research Letters*, 45, 4419–4428, <https://doi.org/10.1029/2018GL077207>, 2018.
- 730  
731 Ham, S. and Hong, S.-Y.: Sensitivity of simulated intraseasonal oscillation to four convective parameterization schemes in a  
732 coupled climate model, *Asia-Pacific J Atmos Sci*, 49, 483–496, <https://doi.org/10.1007/s13143-013-0043-9>, 2013.
- 733  
734 Hansen, F., Matthes, K., and Gray, L. J.: Sensitivity of stratospheric dynamics and chemistry to QBO nudging width in the  
735 chemistry–climate model WACCM, *JGR Atmospheres*, 118, <https://doi.org/10.1002/jgrd.50812>, 2013.
- 736  
737 Hendon, H. H. and Salby, M. L.: The Life Cycle of the Madden–Julian Oscillation, *J. Atmos. Sci.*, 51, 2225–2237,  
738 [https://doi.org/10.1175/1520-0469\(1994\)051<2225:TLCOTM>2.0.CO;2](https://doi.org/10.1175/1520-0469(1994)051<2225:TLCOTM>2.0.CO;2), 1994.
- 739  
740 Hendon, H. H., Zhang, C., and Glick, J. D.: Interannual Variation of the Madden–Julian Oscillation during Austral Summer,  
741 *J. Climate*, 12, 2538–2550, [https://doi.org/10.1175/1520-0442\(1999\)012<2538:IVOTMJ>2.0.CO;2](https://doi.org/10.1175/1520-0442(1999)012<2538:IVOTMJ>2.0.CO;2), 1999.
- 742  
743 Hendon, H. H., Wheeler, M. C., and Zhang, C.: Seasonal Dependence of the MJO–ENSO Relationship, *Journal of Climate*,  
744 20, 531–543, <https://doi.org/10.1175/JCLI4003.1>, 2007.
- 745  
746 Henley, B. J., Gergis, J., Karoly, D. J., Power, S., Kennedy, J., and Folland, C. K.: A Tripole Index for the Interdecadal Pacific  
747 Oscillation, *Clim Dyn*, 45, 3077–3090, <https://doi.org/10.1007/s00382-015-2525-1>, 2015.
- 748  
749 Hourdin, F., Grandpeix, J.-Y., Rio, C., Bony, S., Jam, A., Cheruy, F., Rochetin, N., Fairhead, L., Idelkadi, A., Musat, I.,  
750 Dufresne, J.-L., Lahellec, A., Lefebvre, M.-P., and Roehrig, R.: LMDZ5B: the atmospheric component of the IPSL climate  
751 model with revisited parameterizations for clouds and convection, *Clim Dyn*, 40, 2193–2222, <https://doi.org/10.1007/s00382-012-1343-y>, 2013.
- 752  
753  
754 Huang, K., Richter, J. H., and Pegion, K. V.: Captured QBO-MJO Connection in a Subseasonal Prediction System,  
755 *Geophysical Research Letters*, 50, e2022GL102648, <https://doi.org/10.1029/2022GL102648>, 2023.
- 756



- 757 Jiang, X., Waliser, D. E., Xavier, P. K., Petch, J., Klingaman, N. P., Woolnough, S. J., Guan, B., Bellon, G., Crueger, T.,  
758 DeMott, C., Hannay, C., Lin, H., Hu, W., Kim, D., Lappen, C., Lu, M., Ma, H., Miyakawa, T., Ridout, J. A., Schubert, S. D.,  
759 Scinocca, J., Seo, K., Shindo, E., Song, X., Stan, C., Tseng, W., Wang, W., Wu, T., Wu, X., Wyser, K., Zhang, G. J., and Zhu,  
760 H.: Vertical structure and physical processes of the Madden-Julian oscillation: Exploring key model physics in climate  
761 simulations, *JGR Atmospheres*, 120, 4718–4748, <https://doi.org/10.1002/2014JD022375>, 2015.  
762
- 763 Jiang, X., Maloney, E., and Su, H.: Large-scale controls of propagation of the Madden-Julian Oscillation, *npj Clim Atmos Sci*,  
764 3, 29, <https://doi.org/10.1038/s41612-020-00134-x>, 2020.  
765
- 766 Jin, D., D. Kim, S.-W. Son, and L. Oreopoulos, 2023: QBO deepens MJO convection, *Nature Communications*, 14, 4088,  
767 <https://doi.org/10.1038/s41467-023-39465-7>  
768
- 769 Kang, I.-S., Liu, F., Ahn, M.-S., Yang, Y.-M., and Wang, B.: The Role of SST Structure in Convectively Coupled Kelvin–  
770 Rossby Waves and Its Implications for MJO Formation, *Journal of Climate*, 26, 5915–5930, <https://doi.org/10.1175/JCLI-D-12-00303.1>, 2013.  
771
- 772 Kawatani, Y., Hamilton, K., Sato, K., Dunkerton, T. J., Watanabe, S., and Kikuchi, K.: ENSO Modulation of the QBO: Results  
773 from MIROC Models with and without Nonorographic Gravity Wave Parameterization, *Journal of the Atmospheric Sciences*,  
774 76, 3893–3917, <https://doi.org/10.1175/JAS-D-19-0163.1>, 2019.  
775
- 776 Kelley, M., Schmidt, G. A., Nazarenko, L. S., Bauer, S. E., Ruedy, R., Russell, G. L., Ackerman, A. S., Aleinov, I., Bauer, M.,  
777 Bleck, R., Canuto, V., Cesana, G., Cheng, Y., Clune, T. L., Cook, B. I., Cruz, C. A., Del Genio, A. D., Elsaesser, G. S.,  
778 Faluvegi, G., Kiang, N. Y., Kim, D., Lacis, A. A., Leboissetier, A., LeGrande, A. N., Lo, K. K., Marshall, J., Matthews, E. E.,  
779 McDermid, S., Mezuman, K., Miller, R. L., Murray, L. T., Oinas, V., Orbe, C., García-Pando, C. P., Perlwitz, J. P., Puma, M.  
780 J., Rind, D., Romanou, A., Shindell, D. T., Sun, S., Tausnev, N., Tsigaridis, K., Tselioudis, G., Weng, E., Wu, J., and Yao,  
781 M.: GISS-E2.1: Configurations and Climatology, *J Adv Model Earth Syst*, 12, e2019MS002025,  
782 <https://doi.org/10.1029/2019MS002025>, 2020.  
783
- 784 Kessler, W. S.: EOF Representations of the Madden–Julian Oscillation and Its Connection with ENSO\*, *J. Climate*, 14, 3055–  
785 3061, [https://doi.org/10.1175/1520-0442\(2001\)014<3055:EROTMJ>2.0.CO;2](https://doi.org/10.1175/1520-0442(2001)014<3055:EROTMJ>2.0.CO;2), 2001.  
786
- 787 Kiladis, G. N., Wheeler, M. C., Haertel, P. T., Straub, K. H., and Roundy, P. E.: Convectively coupled equatorial waves,  
788 *Reviews of Geophysics*, 47, 2008RG000266, <https://doi.org/10.1029/2008RG000266>, 2009.  
789
- 790 Kim, D., Xavier, P., Maloney, E., Wheeler, M., Waliser, D., Sperber, K., Hendon, H., Zhang, C., Neale, R., Hwang, Y.-T., and  
791 Liu, H.: Process-Oriented MJO Simulation Diagnostic: Moisture Sensitivity of Simulated Convection, *Journal of Climate*, 27,  
792 5379–5395, <https://doi.org/10.1175/JCLI-D-13-00497.1>, 2014.  
793
- 794 Kim, H., Caron, J. M., Richter, J. H., and Simpson, I. R.: The Lack of QBO-MJO Connection in CMIP6 Models, *Geophysical*  
795 *Research Letters*, 47, e2020GL087295, <https://doi.org/10.1029/2020GL087295>, 2020.  
796
- 797 Kim, J., K. M. Grise, and S.-W. Son, 2013: Thermal characteristics of the cold-point tropopause region in CMIP5 models,  
798 *Journal of Geophysical Research - Atmospheres*, 118, 8827–8841.  
799
- 800 Klotzbach, P., Abhik, S., Hendon, H. H., Bell, M., Lucas, C., G. Marshall, A., and Oliver, E. C. J.: On the emerging relationship  
801 between the stratospheric Quasi-Biennial oscillation and the Madden-Julian oscillation, *Sci Rep*, 9, 2981,  
802 <https://doi.org/10.1038/s41598-019-40034-6>, 2019.  
803
- 804





- 805 Kumar, V., Yoden, S., and Hitchman, M. H.: QBO and ENSO Effects on the Mean Meridional Circulation, Polar Vortex,  
806 Subtropical Westerly Jets, and Wave Patterns During Boreal Winter, *JGR Atmospheres*, 127,  
807 e2022JD036691, <https://doi.org/10.1029/2022JD036691>, 2022.
- 808
- 809 Lawrence, Z. D., Elsbury, D., Butler, A. H., Perlwitz, J., Albers, J. R., Ciasto, L. M., and Ray, E.: Evaluation of Processes  
810 Related to Stratosphere–Troposphere Coupling in GEFsV12 Subseasonal Hindcasts, *Monthly Weather Review*, 151, 1735–  
811 1755, <https://doi.org/10.1175/MWR-D-22-0283.1>, 2023.
- 812
- 813 Lim, Y. and Son, S.: QBO-MJO Connection in CMIP5 Models, *JGR Atmospheres*, 125, e2019JD032157,  
814 <https://doi.org/10.1029/2019JD032157>, 2020.
- 815
- 816 Lin, H.: The Madden-Julian Oscillation, *Atmosphere-Ocean*, 60, 338–359, <https://doi.org/10.1080/07055900.2022.2072267>,  
817 2022.
- 818
- 819 Madden, R. A. and Julian, P. R.: Observations of the 40–50-Day Tropical Oscillation—A Review, *Mon. Wea. Rev.*, 122, 814–  
820 837, [https://doi.org/10.1175/1520-0493\(1994\)122<0814:OOTDTP>2.0.CO;2](https://doi.org/10.1175/1520-0493(1994)122<0814:OOTDTP>2.0.CO;2), 1994.
- 821
- 822 Martin, Z., S.-W. Son, A. Butler, H. Hendon, H. Kim, A. Sobel, S. Yoden, and C. Zhang, 2021: The influence of the Quasi-  
823 Biennial Oscillation on the Madden-Julian Oscillation, *Nature Reviews Earth & Environment*, <https://doi.org/10.1038/s43017-021-00173-9>.
- 824
- 825
- 826 Martin, Z. K., Simpson, I. R., Lin, P., Orbe, C., Tang, Q., Caron, J. M., Chen, C., Kim, H., Leung, L. R., Richter, J. H., and  
827 Xie, S.: The Lack of a QBO-MJO Connection in Climate Models With a Nudged Stratosphere, *JGR Atmospheres*, 128,  
828 e2023JD038722, <https://doi.org/10.1029/2023JD038722>, 2023.
- 829
- 830 Matsuno, T.: Quasi-Geostrophic Motions in the Equatorial Area, *Journal of the Meteorological Society of Japan*, 44, 25–43,  
831 [https://doi.org/10.2151/jmsj1965.44.1\\_25](https://doi.org/10.2151/jmsj1965.44.1_25), 1966.
- 832
- 833 Miura, H., Maeda, T., and Kimoto, M.: A Comparison of the Madden-Julian Oscillation Simulated by Different Versions of  
834 the MIROC Climate Model, *SOLA*, 8, 165–169, <https://doi.org/10.2151/sola.2012-040>, 2012.
- 835
- 836 Nakamura, Y. and Takayabu, Y. N.: Convective Couplings with Equatorial Rossby Waves and Equatorial Kelvin Waves. Part  
837 I: Coupled Wave Structures, *Journal of the Atmospheric Sciences*, 79, 247–262, <https://doi.org/10.1175/JAS-D-21-0080.1>,  
838 2022.
- 839
- 840 Newman, M., Sardeshmukh, P. D., and Penland, C.: How Important Is Air–Sea Coupling in ENSO and MJO Evolution?,  
841 *Journal of Climate*, 22, 2958–2977, <https://doi.org/10.1175/2008JCLI2659.1>, 2009.
- 842
- 843 Nordeng, T.-E.: Extended versions of the convective parametrization scheme at ECMWF and their impact on the mean and  
844 transient activity of the model in the tropics, <https://doi.org/10.21957/E34XWHYSW>, 1994.
- 845
- 846 Pahlavan, H. A., Wallace, J. M., Fu, Q., and Kiladis, G. N.: Revisiting the Quasi-Biennial Oscillation as Seen in ERA5. Part  
847 II: Evaluation of Waves and Wave Forcing, *Journal of the Atmospheric Sciences*, 78, 693–707, <https://doi.org/10.1175/JAS-D-20-0249.1>, 2021.
- 848
- 849
- 850 Pan, D. and Randall, D. D. A.: A cumulus parameterization with a prognostic closure, *Quart J Royal Meteorol Soc*, 124, 949–  
851 981, <https://doi.org/10.1002/qj.49712454714>, 1998.
- 852
- 853 Pang, B., Chen, Z., Wen, Z., and Lu, R.: Impacts of two types of El Niño on the MJO during boreal winter, *Adv. Atmos. Sci.*,  
854 33, 979–986, <https://doi.org/10.1007/s00376-016-5272-2>, 2016.





- 855  
856 Pascoe, C. L., Gray, L. J., Crooks, S. A., Juckes, M. N., and Baldwin, M. P.: The quasi-biennial oscillation: Analysis using  
857 ERA-40 data, *J. Geophys. Res.*, 110, 2004JD004941, <https://doi.org/10.1029/2004JD004941>, 2005.
- 858  
859 Philander, S. G.: *El Niño, La Niña, and the southern oscillation*, Academic Press, San Diego, 293 pp., 1990.
- 860  
861 Pohl, B. and Matthews, A. J.: Observed Changes in the Lifetime and Amplitude of the Madden–Julian Oscillation Associated  
862 with Interannual ENSO Sea Surface Temperature Anomalies, *Journal of Climate*, 20, 2659–2674,  
863 <https://doi.org/10.1175/JCLI4230.1>, 2007.
- 864  
865 Puy, M., Vialard, J., Lengaigne, M., and Guilyardi, E.: Modulation of equatorial Pacific westerly/easterly wind events by the  
866 Madden–Julian oscillation and convectively-coupled Rossby waves, *Clim Dyn*, 46, 2155–2178,  
867 <https://doi.org/10.1007/s00382-015-2695-x>, 2016.
- 868  
869 Randall, D. A., Tziperman, E., Branson, M. D., Richter, J. H., and Kang, W.: The QBO–MJO Connection: A Possible Role  
870 for the SST and ENSO, *Journal of Climate*, 36, 6515–6531, <https://doi.org/10.1175/JCLI-D-23-0031.1>, 2023.
- 871  
872 Richter, J. H., Anstey, J. A., Butchart, N., Kawatani, Y., Meehl, G. A., Osprey, S., and Simpson, I. R.: Progress in Simulating  
873 the Quasi-Biennial Oscillation in CMIP Models, *JGR Atmospheres*, 125, e2019JD032362,  
874 <https://doi.org/10.1029/2019JD032362>, 2020.
- 875  
876 Rind, D., Jonas, J., Balachandran, N. K., Schmidt, G. A., and Lean, J.: The QBO in two GISS global climate models: 1.  
877 Generation of the QBO, *JGR Atmospheres*, 119, 8798–8824, <https://doi.org/10.1002/2014JD021678>, 2014.
- 878  
879 Rind, D., Orbe, C., Jonas, J., Nazarenko, L., Zhou, T., Kelley, M., Lacis, A., Shindell, D., Faluvegi, G., Romanou, A., Russell,  
880 G., Tausnev, N., Bauer, M., and Schmidt, G.: GISS Model E2.2: A Climate Model Optimized for the Middle Atmosphere—  
881 Model Structure, Climatology, Variability, and Climate Sensitivity, *JGR Atmospheres*, 125, e2019JD032204,  
882 <https://doi.org/10.1029/2019JD032204>, 2020.
- 883  
884 Roundy, P. E.: The Spectrum of Convectively Coupled Kelvin Waves and the Madden–Julian Oscillation in Regions of Low-  
885 Level Easterly and Westerly Background Flow, *Journal of the Atmospheric Sciences*, 69, 2107–2111,  
886 <https://doi.org/10.1175/JAS-D-12-060.1>, 2012.
- 887  
888 Sakaeda, N., Dias, J., and Kiladis, G. N.: The Unique Characteristics and Potential Mechanisms of the MJO–QBO Relationship,  
889 *JGR Atmospheres*, 125, e2020JD033196, <https://doi.org/10.1029/2020JD033196>, 2020.
- 890  
891 Schenzinger, V., Osprey, S., Gray, L., and Butchart, N.: Defining metrics of the Quasi-Biennial Oscillation in global climate  
892 models, *Geosci. Model Dev.*, 10, 2157–2168, <https://doi.org/10.5194/gmd-10-2157-2017>, 2017.
- 893  
894 Schreck, C. J.: Global Survey of the MJO and Extreme Precipitation, *Geophysical Research Letters*, 48,  
895 e2021GL094691, <https://doi.org/10.1029/2021GL094691>, 2021.
- 896  
897 Serva, F., Anstey, J. A., Bushell, A. C., Butchart, N., Cagnazzo, C., Gray, L. J., Kawatani, Y., Osprey, S. M., Richter, J. H.,  
898 and Simpson, I. R.: The impact of the QBO on the region of the tropical tropopause in QBOi models: Present-day simulations,  
899 *Quart J Royal Meteorol Soc*, 148, 1945–1964, <https://doi.org/10.1002/qj.4287>, 2022.
- 900  
901 Serva, F., Christiansen, B., Davini, P., Von Hardenberg, J., Van Den Oord, G., Reerink, T. J., Wyser, K., and Yang, S.: Changes  
902 in Stratospheric Dynamics Simulated by the EC-Earth Model From CMIP5 to CMIP6, *J Adv Model Earth Syst*, 16,  
903 e2023MS003756, <https://doi.org/10.1029/2023MS003756>, 2024.
- 904



- 905 Slingo, J. M., Rowell, D. P., Sperber, K. R., and Nortley, F.: On the predictability of the interannual behaviour of the Madden-  
906 Julian oscillation and its relationship with el Niño, *Quart J Royal Meteor Soc*, 125, 583–609,  
907 <https://doi.org/10.1002/qj.49712555411>, 1999.  
908
- 909 Son, S.-W., Lim, Y., Yoo, C., Hendon, H. H., and Kim, J.: Stratospheric Control of the Madden–Julian Oscillation, *Journal of*  
910 *Climate*, 30, 1909–1922, <https://doi.org/10.1175/JCLI-D-16-0620.1>, 2017.  
911
- 912 Straub, K. H. and Kiladis, G. N.: Observations of a Convectively Coupled Kelvin Wave in the Eastern Pacific ITCZ, *J. Atmos.*  
913 *Sci.*, 59, 30–53, [https://doi.org/10.1175/1520-0469\(2002\)059<0030:OOACCK>2.0.CO;2](https://doi.org/10.1175/1520-0469(2002)059<0030:OOACCK>2.0.CO;2), 2002.  
914
- 915 Suematsu, T. and Miura, H.: Zonal SST Difference as a Potential Environmental Factor Supporting the Longevity of the  
916 Madden–Julian Oscillation, *Journal of Climate*, 31, 7549–7564, <https://doi.org/10.1175/JCLI-D-17-0822.1>, 2018.  
917
- 918 Suematsu, T. and Miura, H.: Changes in the Eastward Movement Speed of the Madden–Julian Oscillation with Fluctuation in  
919 the Walker Circulation, *Journal of Climate*, 35, 211–225, <https://doi.org/10.1175/JCLI-D-21-0269.1>, 2022.  
920
- 921 Sun, L., Wang, H., and Liu, F.: Combined effect of the QBO and ENSO on the MJO, *Atmospheric and Oceanic Science*  
922 *Letters*, 12, 170–176, <https://doi.org/10.1080/16742834.2019.1588064>, 2019.  
923
- 924 Tam, C.-Y. and Lau, N.-C.: Modulation of the Madden-Julian Oscillation by ENSO: Inferences from Observations and GCM  
925 Simulations, *Journal of the Meteorological Society of Japan*, 83, 727–743, <https://doi.org/10.2151/jmsj.83.727>, 2005.  
926
- 927 Tegtmeier, S., Anstey, J., Davis, S., Ivanciu, I., Jia, Y., McPhee, D., and Pilch Kedzierski, R.: Zonal Asymmetry of the QBO  
928 Temperature Signal in the Tropical Tropopause Region, *Geophysical Research Letters*, 47, e2020GL089533,  
929 <https://doi.org/10.1029/2020GL089533>, 2020.  
930
- 931 Tiedtke, M.: A Comprehensive Mass Flux Scheme for Cumulus Parameterization in Large-Scale Models, *Mon. Wea. Rev.*,  
932 117, 1779–1800, [https://doi.org/10.1175/1520-0493\(1989\)117<1779:ACMFSF>2.0.CO;2](https://doi.org/10.1175/1520-0493(1989)117<1779:ACMFSF>2.0.CO;2), 1989.  
933
- 934 Vitart, F.: Madden—Julian Oscillation prediction and teleconnections in the S2S database, *Quart J Royal Meteor Soc*, 143,  
935 2210–2220, <https://doi.org/10.1002/qj.3079>, 2017.  
936
- 937 Waliser, D., Sperber, K., Hendon, H., Kim, D., Maloney, E., Wheeler, M., Weickmann, K., Zhang, C., Donner, L., Gottschalck,  
938 J. and Higgins, W. MJO simulation diagnostics. *J. Climate*, 22, 3006–3030, <https://doi.org/10.1175/2008JCLI2731.1>, 2009  
939
- 940 Wang, B., Chen, G., and Liu, F.: Diversity of the Madden-Julian Oscillation, *Sci. Adv.*, 5, eaax0220,  
941 <https://doi.org/10.1126/sciadv.aax0220>, 2019.  
942
- 943 Wang, T. and Li, T.: Diversity of MJO Initiation Regions and Processes, *Journal of Climate*, 35, 3121–3140,  
944 <https://doi.org/10.1175/JCLI-D-21-0816.1>, 2022.  
945
- 946 Wang, Y.-C., Tseng, W.-L., and Hsu, H.-H.: Role of convection–circulation coupling in the propagation mechanism of the  
947 Madden–Julian Oscillation over the Maritime Continent in a climate model, *Clim Dyn*, 58, 2469–2484,  
948 <https://doi.org/10.1007/s00382-021-06013-2>, 2022.  
949
- 950 Wei, Y. and Ren, H.-L.: Modulation of ENSO on Fast and Slow MJO Modes during Boreal Winter, *Journal of Climate*, 32,  
951 7483–7506, <https://doi.org/10.1175/JCLI-D-19-0013.1>, 2019.  
952



- 953 Wheeler, M. C. and Hendon, H. H.: An All-Season Real-Time Multivariate MJO Index: Development of an Index for  
954 Monitoring and Prediction, *Mon. Wea. Rev.*, 132, 1917–1932, [https://doi.org/10.1175/1520-0493\(2004\)132<1917:AARMMI>2.0.CO;2](https://doi.org/10.1175/1520-0493(2004)132<1917:AARMMI>2.0.CO;2), 2004.
- 955  
956
- 957 Yadav, P. and Straus, D. M.: Circulation Response to Fast and Slow MJO Episodes, *Monthly Weather Review*, 145, 1577–  
958 1596, <https://doi.org/10.1175/MWR-D-16-0352.1>, 2017.
- 959
- 960 Yadav, P., Garfinkel, C. I., and Domeisen, D. I. V.: The Role of the Stratosphere in Teleconnections Arising From Fast and  
961 Slow MJO Episodes, *Geophysical Research Letters*, 51, e2023GL104826, <https://doi.org/10.1029/2023GL104826>, 2024.
- 962
- 963 Yoo, C., and S.-W. Son, 2016: Modulation of the boreal wintertime Madden-Julian Oscillation by the stratospheric Quasi-  
964 Biennial Oscillation, *Geophysical Research Letters*, 43, 1392-1398.
- 965
- 966 Yukimoto, S., Kawai, H., Koshiro, T., Oshima, N., Yoshida, K., Urakawa, S., Tsujino, H., Deushi, M., Tanaka, T., Hosaka,  
967 M., Yabu, S., Yoshimura, H., Shindo, E., Mizuta, R., Obata, A., Adachi, Y., and Ishii, M.: The Meteorological Research  
968 Institute Earth System Model Version 2.0, MRI-ESM2.0: Description and Basic Evaluation of the Physical Component,  
969 *Journal of the Meteorological Society of Japan*, 97, 931–965, <https://doi.org/10.2151/jmsj.2019-051>, 2019.
- 970
- 971 Yuni, A. R. E., Lubis, S. W., and Setiawan, S.: Vertical structure of Convectively Coupled Equatorial Waves (CCEWs) during  
972 Boreal Summer and Winter, *IOP Conf. Ser.: Earth Environ. Sci.*, 284, 012010, <https://doi.org/10.1088/1755-1315/284/1/012010>, 2019.
- 973  
974
- 975 Zhang, C. and Gottschalck, J.: SST Anomalies of ENSO and the Madden–Julian Oscillation in the Equatorial Pacific\*, *J.*  
976 *Climate*, 15, 2429–2445, [https://doi.org/10.1175/1520-0442\(2002\)015<2429:SAOEAT>2.0.CO;2](https://doi.org/10.1175/1520-0442(2002)015<2429:SAOEAT>2.0.CO;2), 2002.
- 977
- 978 Zhang, G. J. and McFarlane, N. A.: Sensitivity of climate simulations to the parameterization of cumulus convection in the  
979 Canadian climate centre general circulation model, *Atmosphere-Ocean*, 33, 407–446,  
980 <https://doi.org/10.1080/07055900.1995.9649539>, 1995.
- 981
- 982 Zhu, J., Kumar, A., and Wang, W.: Dependence of MJO Predictability on Convective Parameterizations, *Journal of Climate*,  
983 33, 4739–4750, <https://doi.org/10.1175/JCLI-D-18-0552.1>, 2020.
- 984  
985